



Insights on Mineralogy and Chemistry of Fairview Gold Mine, Barberton Greenstone Belt, South Africa

MOHAMMED ALNAGASHI HASSAN ALTIGANI

Department of Geology of Minerals Wealth, Faculty of Petroleum and Minerals, Alneelain University,
Khartoum, Sudan. Postal Address : 11121, P.O-Box : 12702

Corresponding author: m.alnagashi@gmail.com
Manuscript received: November, 7, 2018; revised: June, 18, 2019;
approved: June, 13, 2020; available online: March, 1, 2021

Abstract - Laser ablation inductively coupled plasma mass spectrometry (LA-ICP-MS) and electron microprobe analysis (EMPA) techniques were used to determine the mineralogy and chemistry of dominant sulphide and associated gold deposits at the Fairview Gold Mine of the Barberton Greenstone Belt (BGB). The rocks and ore mineral associations at the Fairview Mine indicate mesothermal (orogenic) conditions for the gold deposit. The whole rock chemistry of the Fairview Mine reflects calc-alkaline affinities, and felsic provenance is revealed by high SiO_2 , K_2O , Al_2O_3 , and TiO_2 , and low Fe_2O_3 , MgO , Ni , and Cr contents. The mineral assemblages of the Fairview Mine rocks and ores indicate three phases of metamorphisms; regional prograde, thermal, and retrograde metamorphism, which caused zonation and heterogeneity of the ore minerals. The principal ore minerals in this deposit are pyrite, arsenopyrite, pyrrhotite, chalcopyrite, and rare sphalerite, as well as minor gold. The obtained results revealed that sulphides of the Fairview Mine are divided into two types (generations) varying in their morphology, association, and elemental composition. The old type 1 is porous, anhedral, heterogeneous, contains inclusions and rich in As, Ni, Co, and Au compared to type 2. Trace-element distribution and occurrence mode of gold at Fairview mine reflect two phases of gold mineralization. The first stage is associated with sulphides (mainly pyrite and arsenopyrite), whilst the second phase is free-lode hosted by silicates (mainly quartz).

Keywords: Barberton Greenstone Belt, Fairview Gold Mine, EMPA, LA-ICP-MS, pyrite

© IJOG - 2021

How to cite this article:

Altigani, M. A. H., 2021. Insights on Mineralogy and Chemistry of Fairview Gold Mine, Barberton Greenstone Belt, South Africa. *Indonesian Journal on Geoscience*, 8 (1), p.73-99. DOI: [10.17014/ijog.8.1.73-99](https://doi.org/10.17014/ijog.8.1.73-99)

INTRODUCTION

Background

There are large numbers of greenstone belts in the world, about 260 of them are of Archaean age. The name 'greenstone' reflects the dominantly basaltic volcanic and intrusive rocks of low metamorphic grade (Goldfarb *et al.*, 2001; Furnes *et al.*, 2010). The Kaapvaal Craton (Figure 1) in Southern Africa underlies most of the northern

part of South Africa, Swaziland, and a small part of eastern Botswana (Bumby *et al.*, 2011). It is considered as one of the oldest and best-preserved Archaean continental fragments on earth (Dirks *et al.*, 2013). It was accumulated between 3 and 2.7 Ga and contains rocks as old as 3.7 Ga (Goldfarb *et al.*, 2001; Poujol *et al.*, 2003; Schmitz *et al.*, 2004). Uranium/lead (U/Pb) zircon ages in the ancient Gneiss Complex in the Swaziland range from about 3.64 to 3.2 Ga. Neodymium (Nd) model

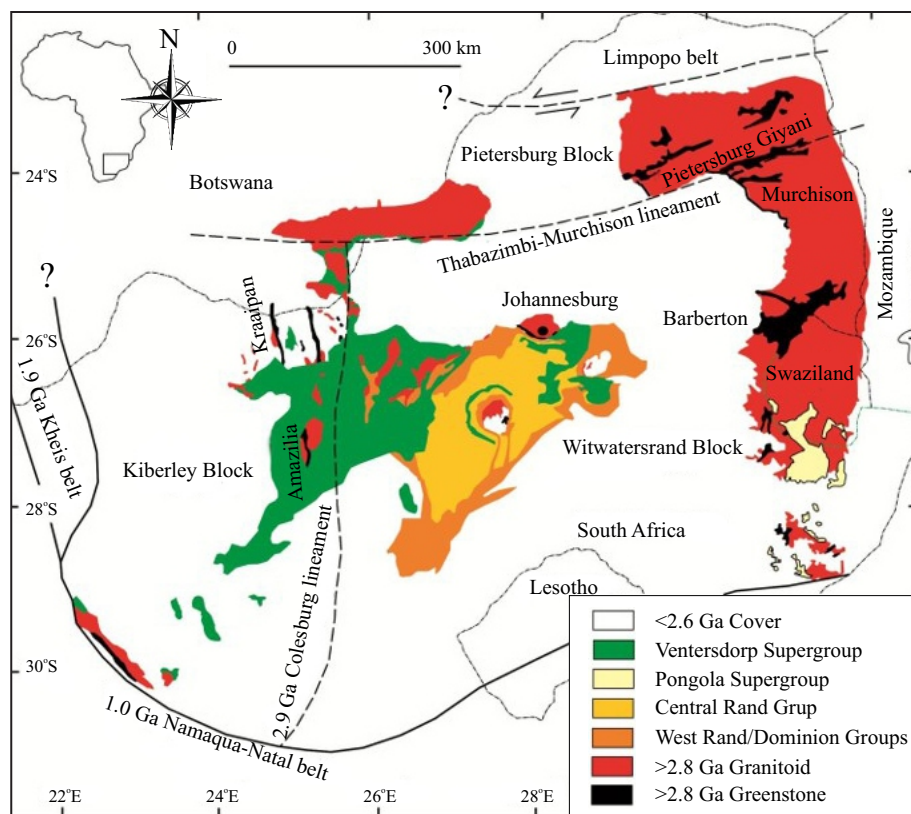


Figure 1. Distribution of the main Archaean stratigraphic units of the Kaapvaal Craton. The Witwatersrand Basin fill comprises the West Rand and the Central Rand Groups; also shown is the outline of the three crustal blocks that are believed to have amalgamated by 2.8 Ga to form a single craton (Frimmel, 2005).

ages suggest that some crust may have formed in this region at 3.8 Ga (Kranendonk *et al.*, 2007). The assembly of the Kaapvaal Craton of South Africa during the Archaean took place episodically over a 1,000-million-year period (3.5 to 2.5 Ga) (Kranendonk *et al.*, 2007). It involved several processes of magmatic arc formation and accretion, as well as tectonic amalgamation of numerous discrete terrains and blocks (De Wit *et al.*, 1992; Lowe, 1994; Poujol and Robb, 1999). However, Kranendonk (2011) tentatively suggested an arc association for the Barberton Greenstone Belt because of noncalc-alkaline geochemical affinity of the Barberton Greenstone Belt felsic volcanics.

The Neoproterozoic-to-Paleoproterozoic Barberton Greenstone Belt (BGB) is found on the Kaapvaal Craton (Yoshihara and Hamano, 2004; Brandl *et al.*, 2006; Kranendonk *et al.*, 2007). The BGB occupies an area of 120 × 50 km², and is situated some 366 km to the east of Pretoria, and 45 km south of Nelspruit near the eastern

margin of the Kaapvaal Craton (Figure 2) (Yoshihara and Hamano, 2004; Brandl *et al.*, 2006). The BGB comprises a region of an exceptional three-dimensional exposure and represents the Archaean crustal evolution (Kranendonk *et al.*, 2007). The BGB consists of tectonically and stratigraphically inserted, NE-striking volcanic and clastic rocks (3.55 - 3.22 Ga) with a thickness of 12 to 15 km (Stiegler *et al.*, 2010), or even 20 km thick (Kranendonk, 2011), surrounded by granite-gneiss domes with the age of 3.5 Ga to 3.1 Ga (Dirks *et al.*, 2013).

Structural studies, which have been carried out on the Archaean gold deposits, indicate that most of these deposits are controlled by open fractures at four places: the shear zone junctions, in drag folded sites, in zones of mashing and contortion of the schist, and at (or near) flexures in the walls of shear zone breccia (Grooves and Foster, 1991). The systematic alignment of the gold deposits suite within shear planes reflects that mineraliza-

tion formed during a single tectonic stage (Dirks *et al.*, 2013).

The physical effects of structural disturbance are caused by structural porosity that increases the volume at the junction areas and creates space for the precipitation of minerals (Bliss, 1992; McCaffrey *et al.*, 1999). At the vicinity of flexures, differential movement along the shear zone causes dilation. Drag folding has the same effect (Bliss, 1992).

The episode of gold deposition is associated with the second and third order structures (D_2 and D_3) (Pitfield and Campbell, 1996; Mhlanga, 2002). Recently, Dirks *et al.* (2013) proposed that the principal stage of gold enrichment in the BGB occurred after tectonic and thermal steadiness of the crust during stabilization of the Kaapvaal Craton. They suggest that brittle-ductile shear zones gave the chance for the deeply mineralized fluids to exist during cratonic extensions.

The Barberton Greenstone Belt is generally characterized by low-grade metamorphism. How-

ever, the metamorphic grade increases towards the sheared contacts with surrounding tonalite-trondhjemite granitic gneisses. These contacts have been interpreted as an extensional interval that separates the greenstone belt from mid-crustal basement gneisses (Diener *et al.*, 2005; Kisters *et al.*, 2010). At least three types of metamorphism (Cloete, 1999) have influenced the rocks of the Barberton Greenstone Belt: sea-floor metamorphism ($M_0 \approx D_0$), burial metamorphism ($M_1 \approx D_0 - D_1$), and dynamic (retrograde) metamorphism ($M_2 \approx D_2 - D_3$).

There are several operating gold mines in the BGB, which include the Fairview Mine. The Fairview Gold Mine consists of greywackes, metapelites, and arkoses, which hosting pyrite, arsenopyrite, pyrrhotite, chalcopyrite, and rarely sphalerite as major domains, and loellingite, neck-line, gersdorffite as minor phases (Otto *et al.*, 2007; Dziggel *et al.*, 2007) (Figure 2). These rocks have been subjected to long periods of metamorphism and deformation, which affected the chemistry of the ore deposits at the Fairview Mine.

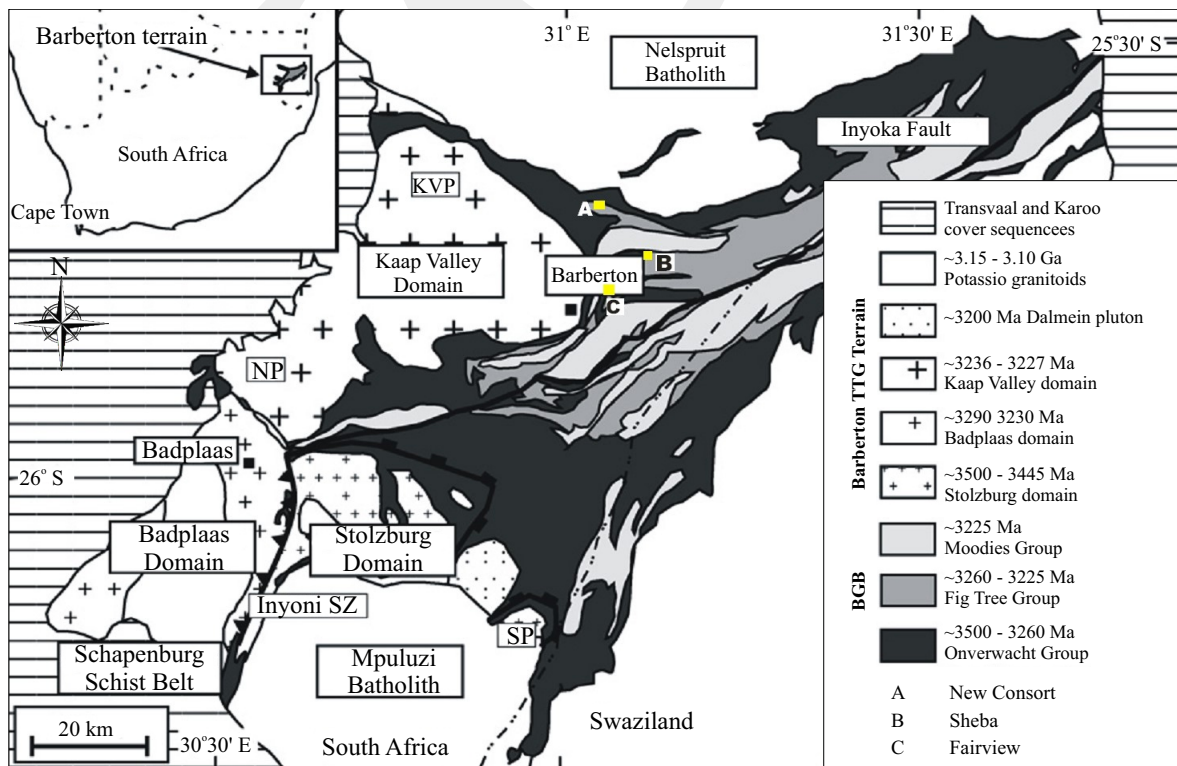


Figure 2. Geological map of the Barberton Greenstone Belt and surrounding granitoid terrains. Also shown are the locations of the major active gold mines (Kisters *et al.*, 2010).

Geological Settings

Archaean greenstone belt, where the Barberton Greenstone Belt (BGB) forms part of, represents essential contributors in world gold production. In this belt, the geological setting of the original source of mineralization (mafic rocks) coupled with the high sensitivity of these rocks to metamorphism, and hydrothermal alterations complicate the determination of the genesis and characteristics of gold deposits associated with these greenstone belts (Kranendonk *et al.*, 2007). Understanding of the influences of mineral associations, metamorphism, deformation, and alterations on these intensively reworked and stressed rocks which are definitely have been subjected to multiple phases of gold and sulphide mineralization, is very important in order to characterize and distinguish the criteria of gold and associated sulphides within these deposits.

The assembly of the Kaapvaal Craton of South Africa during the Archaean took place episodically over a 1,000-million-year period (3.5 to 2.5 Ga) (Kranendonk *et al.*, 2007). It involved several processes of magmatic arc formation and accretion, as well as tectonic amalgamation of numerous discrete terrains and blocks (De Wit *et al.*, 1992; Lowe, 1994; Poujol and Robb, 1999). However, Kranendonk (2011) tentatively suggested an arc association for the Barberton Greenstone Belt because of noncalc-alkaline geochemical affinity of the Barberton Greenstone Belt felsic volcanics.

Neoproterozoic to Paleoproterozoic volcano-sedimentary sequences cover most of the Kaapvaal Craton (Figure 1). One of these is the Barberton Greenstone Belt (BGB), which comprises a region of an exceptional three-dimensional exposure and represents the type area for Archaean crustal evolution on the Craton (Kranendonk *et al.*, 2007). The BGB consists of tectonically and stratigraphically inserted, NE-striking volcanic and clastic rocks (3.55 - 3.22 Ga) with a thickness of 12 to 15 km (Stiegler *et al.*, 2010), or even 20 km thick (Kranendonk, 2011), surrounded by granite-gneiss domes with the age of 3.5 Ga to 3.1 Ga (Dirks *et al.*, 2013). The Barberton

Greenstone Belt is one of the most studied Early Archaean greenstone belts and is considered one of the oldest granite-greenstone belts worldwide (Kranendonk *et al.*, 2007), belonging to the Swazian Era (3.6 - 3.1 Ga) (Kamo and Davis, 1994; Kroner *et al.*, 1996; Brandl *et al.*, 2006).

Rocks of the Barberton Greenstone Belt stratigraphically belong to the Barberton Supergroup (Viljoen and Viljoen, 1969; Kent, 1980; Ward, 1995; Ward, 1999; Brandl *et al.*, 2006), which comprises three major lithostratigraphic units (from older to younger):

1. The Onverwacht Group (ca. 3.49 - 3.45 Ga; Eriksson *et al.*, 2001) comprises largely ultramafic to mafic volcanic rocks, dated by Kranendonk *et al.* (2007) between 3.55 and 3.3 Ga. The Onverwacht consists of komatiites, komatiitic basalts, basalts and pillow lavas, minor felsic volcanics, and sedimentary rocks (such as chert beds), which formed in a deep to shallow marine environment (Eriksson *et al.*, 2001; Hofmann, 2005). De Wit *et al.* (2011) suggested that the Onverwacht Formation was subdivided into seven geological complexes, which were separated by at least seven major shear zones. These geological units are the Sandspruit Complex, the Theespruit Complex, the Komati Complex, the Hooggenoeg Complex, the Noisy Complex [3432 ±10 Ma. (Grosch *et al.*, 2011)], the Mendon Complex, and the Kromberg Complex.
2. The Fig Tree Group (3.260 - 3.226 Ga) is a metaturbiditic succession (Hofmann, 2005), up to 2,000 m thick (Eriksson *et al.*, 2001), and consists mainly of greywackes, shale, chert, and dacitic rocks. Five formations have been distinguished north of the Inyoka Fault namely the Ulundi, Sheba, Belvue Road, Bien Venue, and Schoongezicht Formations (Hofmann, 2005).
3. The Moodies Group (3.227±1 Ga) is characterized by arenaceous rocks (Hofmann, 2005; Kranendonk *et al.*, 2007), consisting of conglomerates, sandstones, siltstones,

and shale. The Moodies group sequence is approximately 3,000 m thick, consisting of conglomerates or pebbly sandstones at the base, a thick sandstone unit in the middle, and siltstones, wackes, shale, and banded iron formation (BIF) at the top (Eriksson *et al.*, 2001; Kranendonk *et al.*, 2007).

The Moodies Group was deposited in a shallow marine to fluvial environment, prior to the emplacement of the Kaap Valley tonalite plutons (Figure 2), which has been dated after (Kamo and Davis, 1994). Eriksson *et al.* (1997) and Eriksson *et al.* (2001) suggested braided fluvial, littoral, and shelf depositional systems for the Moodies sedimentary rocks.

METHODOLOGY

Gold and associated sulphides in the Fairview Mine have been studied using microscopic and analytical methods, which are mentioned below. The methods were applied to determine mineralogical, chemical characterizations of gold deposits, and their association timing of ore mineralization. These techniques are transmitted, ore, and SEM (Scanning Electron microscopies), Electron Microprobe Analysis (EMPA), and Laser Ablation-inductively Coupled Plasma-Mass Spectrometry (LA-ICP-MS). The samples used in this study were sponsored by Forensic Laboratory, Pretoria, South Africa, and were collected from Fairview Mine, which is located in the Barberton Greenstone Belt.

Microscopy

For the microscopic investigations, polished and thin sections were prepared at the Geology Department, University of Pretoria. These sections were studied using a conventional transmitted and reflected light microscope in order to determine the mineral assemblages using point counting for % mineral proportion, textural and microstructural characteristics, the degree of alteration, and the metamorphic grade of the rock

units. Representative samples were selected for chemical analyses after microscopic examinations. Finally, the mineral parageneses, textures, and structures of the ores were also investigated.

X-Ray Diffraction Analysis

For the XRD analysis, ten grams from each sample were ground following the standard procedure. They were examined using the X-Ray diffractometer model 'PANalytical X'Pert PRO'. The measurements were performed at the Department of Geology, University of Pretoria, on a Panalytical X'Pert PRO X-ray diffractometer in θ - θ configuration, equipped with a Fe filtered Co-K α radiation (1.789Å) and with an X'Celerator detector and variable divergence- and receiving slits. Samples were prepared according to the standardized Panalytical back loading system, which provides nearly random distribution of the particles.

The data were collected in the angular range $5^\circ \leq 2\theta \leq 90^\circ$ with a step size $0.008^\circ 2\theta$. The phases were identified using X'Pert Highscore Plus software. Errors are on the 3-sigma level, Amorphous phases (if present) were not taken into consideration in the quantification.

The relative phase amounts (weight %) were estimated by the Rietveld method using Autoquan/BGMN software (GE Inspection Technologies; Kleeberg & Bergamnn) employing Fundamental Parameter Approach. In the Rietveld Method, an observed data pattern was compared to a calculated pattern. By variation of all parameters, the difference between the calculated and observed pattern was then minimized by a least square procedure, until the best possible fit is obtained.

X-Ray Fluorescence Analysis

The samples were analyzed using the pressed powder technique based on the method described by Watson (1996). Ten to 12 grams (75% <63 μ m) were taken from each sample and mixed with ten drops of polyvinyl alcohol (48 - 80) saturated solution (as binder), added to each sample powder, then loaded into collapsible aluminium

cups (diameter 40 mm) and pressed by a manual oil-hydraulic press under 20 ton/cm² for two minutes. The Cr-steel piston (diameter 40 mm) was levelled by polishing. The samples are then dried at 110°C before analysis.

The analyses were performed using the wavelength dispersive X-Ray Fluorescence Spectrometer (PANalytical) model “ARL 9400XP+”. The analyses were executed using the computer software “UniQuant”. In this study, only elements found above the detection limits have been reported. The data reduction software reports the results of all elements above the lower limit of detection. Due to the calculation procedure in “UniQuant”, the data are reported normalized to 100. The quantification of the analyses was obtained by analyzing certified standard materials as references.

Scanning Electron Microscopy-Energy Dispersive Spectroscopy (SEM-EDS) Analysis

The polished sections used in this study were coated with carbon with a thickness of approximately 40Å, which allows dispersion of charging during the SEM analyses. A silver strip was used for conduction between carbon coating on the sample and the sample holder during the analysis.

The scanning microscope instrument, model ‘JEOL JSM-5800V’ of the Physics Department at University of Pretoria, was used to investigate the samples in this research. This task was done by using an accelerating potential of 20 kV. Semi-quantitative chemical analyses were performed using the Energy Dispersive Spectroscopy (EDS, X-Raytech). Sample photos were taken with the help of the ‘Orion 6.60.4’ programme, and semi-quantitative analyses were carried out using the ‘NSS-X-Ray’ microanalysis software.

EMPA

In this study, imaging and elemental analyses were performed (using the ‘CAMECA VX 100’ electron microprobe) on the gold and sulphide ores from the Fairview Mine. The standard procedures at the University of Pretoria were followed, which were based on Reed (2005).

The samples were repolished on nylon pads with a series of diamond powder to 0.25 µm finish. Atomic number, absorption, and fluorescence were processed by ZAF corrections. Quantification analysis of the samples was performed with an accelerating voltage of 20 kV, a current of 20 nano ampere (nA), and a focused spot (<1 µm diameter). Count times, for all elements, were 10 seconds. Mineral matrix matched standards were used for calibration.

LA-ICP-MS

Laser Ablation Inductively Coupled Plasma Mass Spectrometry (LA-ICP-MS) is favoured in many geological studies including ore mineral identification because of its high range of sensitivity, high precision, low detection limits, and relatively analysis large sample volume compared with EMPA, which mainly examines sample surface (Sylvester *et al.*, 2005; Humayun *et al.*, 2010; Shaheen *et al.*, 2012). The LA-ICP-MS technique requires minimal sample preparation (Shaheen *et al.*, 2012). In LA-ICP-MS, the sample is directly analyzed by spot ablating with a pulsed laser beam. The created aerosols are transported into the core of inductively coupled argon plasma (ICP), at a temperature of approximately 8,000°C (Thomas, 2005). The plasma in the ICP-MS is used to generate ions, which are introduced to the mass analyzer. The ions are separated and collected to their mass values and charge ratios accordingly. The LA-ICP-MS has a higher sensitivity than the EMPA and is probably able to detect concentrations below one part in 10¹² (part per trillion) (Sylvester, 2008).

In this research, an Agilent Technologies model ‘ICP-MS 7500 Series’ instrument was used at the South African Police Forensic Science Laboratory, Pretoria, South Africa. This machine is equipped with a high-performance NEW WAVE model UP-213 laser ablation system. This system is presently considered the best type to reduce and minimize the inter-elemental fractionation that could be caused by local temperature changes, ablation time, and variations in the matrix matched elements (Chen, 1999; Gaboardi and Humayun,

2009, Woodhead *et al.*, 2009). The fluency value of the laser beam is $> 30 \text{ j/cm}^2$.

The samples were placed in the ablation cell, and the aerosol produced by ablation was swept into the mass spectrometer using a stream of ultrahigh purity He gas (800 ml/min). A stream of Argon gas with flow rate of $\sim 900 - 1,400 \text{ ml/min}$. was added downstream to achieve the differential flow needed to obtain a bright, stable signal. A CCD (charge-coupled device) camera allows imaging of the sample during ablation. The operating MEOLaser 213 software was used to analyze the trace elements in the sulphides and gold of the Fairview Mine of the BGB. The radio frequency (RF) power was 1200 Watt, and the carrier gas (optional gas 95%, 0.90 - 0.95 l/min.). The laser ablation power was 50% with 15 second delay time; the consistent spot size and depth was $25 \mu\text{m}$ with 10 Hz pulse repetition rate and 100% power output. The spots were each ablated for 45 seconds to reduce the possible inter-elemental fractionation.

The machine performance of the LA-ICP-MS was calibrated with international standards as mentioned in Sylvester (2008). The operational parameters were optimized using argon (Ar) gas blanks, and NIST glasses 610 and 612 before starting analyzing an individual mineral grain. The procedure was also repeatedly applied during large numbers of analyses in large grains. The selection of these materials instead of pure gold and sulphide standards is because the optimization requires a creation of steady state signals, and continuous ablation of gold and sulphides may result in coating the core of the laser cell which contaminates the system for a significant time (Watling and Herbert, 1994). The use of NIST glasses is applicable and suitable for measuring reproducibility and instrumental optimization (Watling and Herbert, 1994). Sylvester (2008) suggested that NIST 610 glass might be used to measure concentrations of Cu, Zn, Ag, Pt, and Au in sulphides with an accuracy of 10% using Fe as the internal standard. However, this line of analysis is not approached due to the effects of small amount of impurities in the pyrite which

disturb the ablation rates even if the same matrixes are used.

After analyses, the raw data were cleaned from the background noise by subtracting the blank count per second values from the data for the same spots. The first fifty analyses were omitted from the data set to avoid any background noise.

Glass, gold, and sulphides are not the same material. That means the plasma loading will vary between the three materials; the technique used in this research was not based on the quantification or absolute values of the analyzed elements, but on their counts per second. Once the calibration had been accomplished, reference blanks were also analyzed using the same analytical conditions, and then subtracted from the results. LA-ICP-MS technique used in this study is a less standard technique, and it is highly recommended to verify comparability of the element associations in the samples with data from previous analyses at the same areas (Watling and Herbert, 1994).

RESULTS

Rock Types

Arkoses

These rocks mainly consist of quartz 35 - 67.5 wt. % (Table 1). The quartz is found in four different types: (1) the first is angular and fragmented quartz. (2) The second is medium- to coarse-grained deformed crystals which show kidney-shaped and augen deformational microtextures. (3) The third type is small posttectonic polygons that are located in the pressure shadows of the sulphides (mainly pyrite). (4) The rounded to subrounded quartz represents the fourth type. The Moodies sedimentary rocks are made up of poorly sorted, angular to subrounded clasts with diameters exceeding 25 cm (Eriksson, 1978).

Muscovite (fuchsite) is subdominant, associated with small calcite veins, and ranging from 28.2 wt. % to 42.2 wt. % of these rocks (Table 1). Muscovite is also found as radial lepidoblastic laths and small sheets situated in pressure shadows of the large quartz and sulphide porphyroblasts. Do-

Table 1. Representative Quantitative XRD Analyses of the Fairview Mine samples (error at the 99.7 % confidence)

Mineral/Sample	125208	125483	125484	125485	125486
Quartz	51.3±1.6	51.9±1.1	32±1.4	49.7±1.5	-
Muscovite	26.5±1.7	28±1.1	50±1.8	39.4±1.7	42.2±1.2
Biotite	-	-	3.2±2	2.6±1.9	-
Dolomite	-	16±0.9	-	-	-
Chlorite	-	-	-	3.7±1.1	4.5±1.3
Pyrite	7.1±0.6	3.9±0.4	6.1±0.7	-	-
Arsenopyrite	-	-	-	4.5±0.5	3.8±0.7
Magnetite	5.89±0.57	-	-	-	-

lomite is a common secondary component within these rocks; epidote and chlorite are rarely found and represent the accessory minerals (Hofmann, 2005). The quartz-mica schists dominate all the lithology of the Fairview Mine. These schists and slates mineralogical and structural characteristics are similar to those described by Kohler and Anhaeusser (2002).

Greywackes

These rocks are considered to be generated from impure calcareous sandstones and are composed of quartz (28.4 - 57.6 wt. %) with an augen microtexture. Carbonate minerals are represented by calcite and dolomite (5.3 - 11.2 wt. %). Green muscovite (fuchsite) (28.2 - 33.9 wt. %) follows the foliation planes, and is situated at pressure shadows. In some samples, it was found as radial large patches.

Metapelites

These rocks are made up of biotite (3.2 - 15 wt. %) which formed after amphiboles as well as actinolite (up to 25.5 wt. %) as radial fibres. Albite shows some deformation microstructures, such as tapered and conjugate lamellae. Muscovite, quartz, sphene, epidote group minerals, and chlorite are present in rare amounts.

TAS variation diagrams (Middlemost, 1994) reflect that the majority of the Fairview Mine rocks were derived from felsic to intermediate igneous rocks (granodiorites and/or dacites-rhyolites). This is also confirmed by the high values of SiO₂, Al₂O₃, K₂O, TiO₂, Rb/Sr, Zr, and Ba (Table 2), and the low values of CaO, Na₂O, Ni, Fe₂O₃, and MgO. The calc-alkaline geochemical affinity of Fairview Mine, suggesting these metavolcano-

sedimentary sequences had deposited in back-arc basins (Raymond, 2002).

Rock Chemistry

The Fairview rocks display a dacitic to rhyodacitic composition (Figure 3) with respect to the major element composition (Hofmann, 2005). The geochemical characteristics of the Fairview Mine indicate a calc-alkaline affinity for these rocks.

SiO₂ contents have a range of 37.4 - 75.3 wt. % (the average is 59.3 wt. %). Al₂O₃ values are relatively low (the average is 14.8 wt. %). K₂O and TiO₂ values are positively related (Figure 3c). The MgO content ranges between 1.4 - 7.8 wt. % (the average is 3.7 wt. %). Fe₂O₃ values are higher than 10 wt. % which are consistent with values from other Archaean terrain (McLennan, 1983). The CaO values in most of these samples are very low, with an average of 2 wt. %. However, two of the samples from the Fairview Mine have relatively high values of CaO (6.1 and 3.3 wt. %). Greywackes show a dacitic to rhyodacitic composition in the major element chemical composition (Toulkeridis *et al.*, 1999).

Most of the high field strength elements (HFSE) such as Zr, Hf, Ta, Nb, and Y are depleted in the Fairview greywackes relative to other Archaean greywackes and to post-Archaean greywackes (Condie, 1993). The greywacke plots localize close to the igneous trend, between the weathering trends of the basaltic and granitic rocks (Figure 4). The sample trends toward Al₂O₃ in this diagram do not indicate weathering processes. Based on Figure 4, no clear chemical weathering is found, and the shifting of the samples towards CaO area reflects later carbonization processes. This was observed in

Table 2. Representative XRF Analyses of the Fairview Mine's Rocks, in wt. %

Sample	125483	125484	125485	125486	125487	125488	125489	125940	125943	125944	EGM-87912	EGM-87913
Na ₂ O	0.239	0.216	0.064	0.156	0.084	0.152	0.135	0.16	0.796	0.038	0.318	0.587
MgO	3.494	5.834	2.077	0.999	3.739	1.234	1.211	1.479	5.107	5.675	0.909	1.567
Al ₂ O ₃	12.279	19.35	15.804	19.477	14.78	13.357	19.171	17.982	5.623	4.992	23.622	23.953
SiO ₂	62.131	49.114	65.212	63.959	64.58	50.804	57.171	60.512	67.035	22.964	53.852	56.931
P ₂ O ₅	0.058	0.113	0.038	0.032	0.044	0.024	0.021	0.022	0.015	0.068	0.015	0.024
K ₂ O	3.105	0.231	4.039	5.043	4.118	2.809	4.547	4.557	1.523	0.886	5.86	6.041
CaO	5.945	0.676	0.546	0.101	1.5	0.101	0.366	0.239	0.363	2.985	0.081	1.463
TiO ₂	0.469	0.049	0.523	0.625	0.554	0.339	0.589	0.605	0.234	0.081	0.817	0.722
V ₂ O ₅	0.03	0.198	0.032	0.04	0.036	0.02	0.034	0.035	0.023	0.006	0.064	0.099
Cr ₂ O ₃	0.162	0.244	0.134	0.142	0.149	0.084	0.141	0.14	0.258	0.023	0.378	0.994
MnO ₂	0.24	14.513	0.07	0.011	0.178	0.003	0.032	0.041	0.054	1.088	0.008	0.083
Fe ₂ O ₃	6.746	0.02	5.834	4.223	6.016	12.358	7.245	6.651	9.191	38.416	5.585	4.174
Co	0.017	0.091	0.021	0.016	0.027	0.028	0.017	0.013	0.036	0.037	0.014	0.026
Ni	0.042	0.012	0.037	0.039	0.041	0.025	0.04	0.043	0.075	0.044	0.074	0.14
Cu	0.011	0.018	0.012	0.011	0.006	0.007	0.013	0.018	0.018	0.105	0.007	0.012
Zn	0.013	0.003	0.006	0.009	0.01	0.005	0.006	0.024	0.013	0.007	0.014	0.04
Ga	0.001	-	0.001	0.002	0.002	0.001	0.001	0.002	0.001	0.001	0.003	0.002
As	0.335	0.512	3.398	1.985	1.362	9.435	3.474	4.301	4.47	2.291	5.466	1.231
Br	-	-	0.003	0.001	0.001	0.001	0.003	0.002	0.004	-	0.003	0.001
Rb	0.011	0.018	0.013	0.017	0.014	0.009	0.015	0.004	0.005	0.002	0.005	0.023
Sr	0.013	0.004	0.002	0.001	0.007	0.008	0.003	0.016	0.007	0.002	0.02	0.006
Y	0.005	0.007	0.005	0.006	0.005	-	0.005	0.002	0.002	0.001	0.003	0.006
Zr	0.015	0.017	0.02	0.021	0.019	0.004	0.015	0.006	0.004	0.003	0.007	0.009
Nb	-	0.001	0.001	0.001	0.001	0.012	-	0.016	-	0.002	0.017	-
Ag	0.001	0.001	0.001	0.002	0.001	0.001	0.001	0.002	0.001	0.001	0.001	0.003
Cd	0.001	0.002	0.001	0.001	-	0.001	-	0.001	0.001	0.001	0.001	0.002
Sb	-	0.002	-	0.001	-	0.001	0.003	0.002	0.006	0.001	-	-
Te	0.002	0.001	0.003	0.002	0.004	0.001	0.001	0.001	0.004	0.001	0.003	0.003
I	0.003	0.004	0.001	0.004	0.014	0.01	0.002	0.005	0.012	0.001	0.001	0.038
Cs	0.001	0.044	0.038	0.038	0.001	0.003	0.039	0.001	0.004	0.005	0.001	0.004
Ba	0.004	0.015	0.004	0.002	0.035	0.014	0.003	0.037	0.011	0.001	0.001	0.001
La	0.027	0.003	0.01	0.01	0.006	0.007	0.001	0.008	0.003	0.001	0.043	0.003
Ce	0.003	0.006	0.013	0.007	0.009	0.002	0.002	0.003	0.003	0.002	0.003	0.006
Pr	0.007	0.018	0.002	0.007	0.002	0.012	0.011	0.013	0.011	0.006	0.002	0.004
Sm	0.003	0.001	0.001	0.002	0.006	0.006	0.004	0.002	0.003	0.007	0.002	0.002
WO	0.002	-	0.001	0.039	0.001	0.045	0.003	0.002	0.009	-	0.002	0.025
Hg	0.003	0.001	0.005	0.001	0.002	0.001	0.048	0.01	0.007	0.007	0.001	-
Tl	0.001	0.001	0.001	0.004	0.003	0.01	0.002	0.002	0.002	0.025	0.03	0.001
Pb	0.053	0.001	0.001	0.002	0.001	0.009	0.003	0.003	0.002	0.001	0.001	0.002
Bi	0.002	0.002	0.001	0.001	0.001	0.003	0.008	0.001	-	0.002	0.007	-
Th	0.001	0.001	0.001	-	-	0.001	0.002	0.001	-	-	0.002	0.001
B	0.003	0.001	-	0.002	-	0.001	0.001	-	0.001	0.002	0.002	0.002
Sc	0.001	-	0.002	0.003	0.002	-	0.001	0.002	0.002	-	-	-
Ru	0.005	0.003	0.002	0.004	0.008	0.001	-	0.006	0.008	0.001	-	0.001
Pd	-	0.005	0.007	0.001	0.006	0.001	0.002	0.004	0.001	0.001	0.005	-
Yb	0.005	0.001	0.004	0.003	0.002	0.003	0.005	0.001	0.006	0.001	0.004	0.007
Pt	-	0.007	0.001	0.001	-	0.001	0.005	0.002	0.001	0.004	0.007	0.007
Au	0.006	0.002	0.003	0.008	0.006	0.028	0.014	0.013	0.015	-	0.021	0.006
Rh	0.001	0.005	0.007	0.004	-	0.001	-	0.004	0.008	0.001	0.004	-
Ir	-	-	0.001	0.001	0.002	-	-	0.002	0.001	0.005	-	-

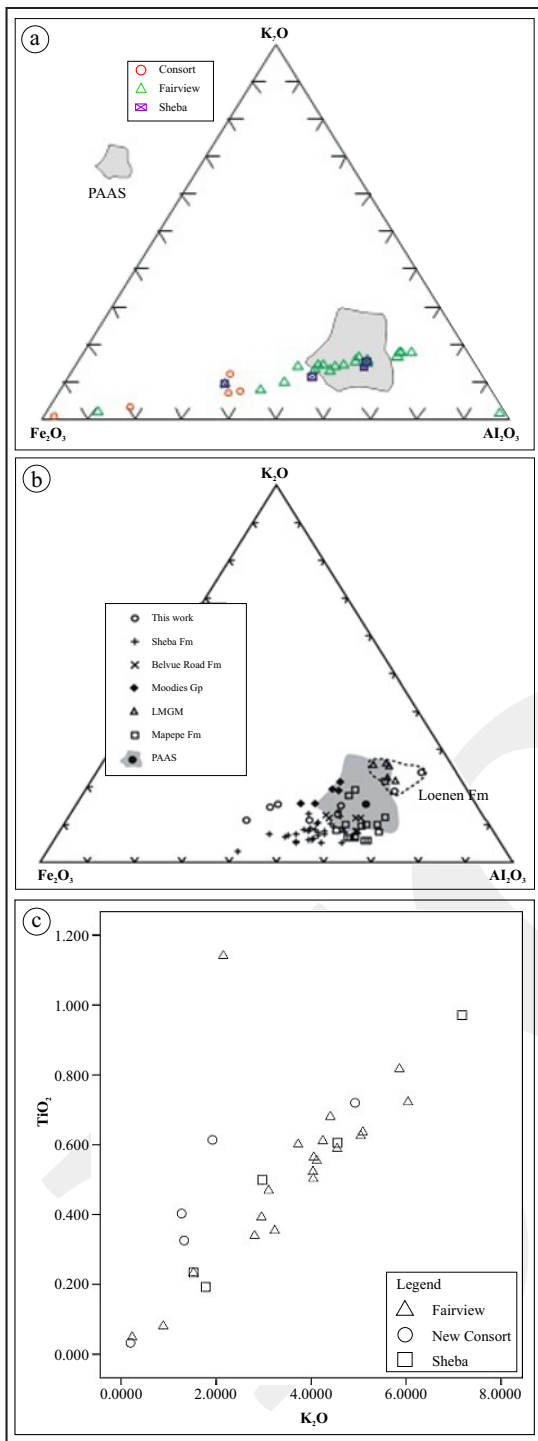


Figure 3. Fe₂O₃-K₂O-Al₂O₃ diagram (after Hofmann, 2005) showing: (a). the distribution of shales and greywackes from Sheba, Fairview, and New Consort Mines from the BGB; (b). Field for PAAS (post Archaeon average Australian shale). Nance and Taylor (1979); whilst (c). K₂O vs. TiO₂ correlation diagram showing these elements are exciting in mica of the Sheba Mine rocks.

the rock thin sections by the presence of carbonate minerals such as dolomite, ankerite, and calcite.

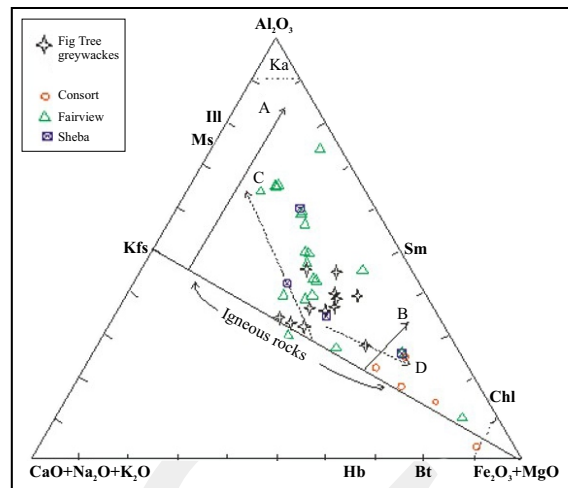


Figure 4. Ternary diagram of molecular Al₂O₃-(CaO+Na₂O+K₂O)-(FeO+MgO), indicate weathering trends of granitic source (A) and basaltic source (B). C= digenetic and/or metasomatic transformation of kaolinite (Ka) into illite (Ill) with fluids characterized by high K⁺/H⁺ ratios. D= digenetic and/or metasomatic transformation of kaolinite into chlorite (Chl) with fluids characterized by high Mg⁺²/H⁺ ratios. Bt= biotite; Kfs= feldspar; Hb= hornblende; Ms= muscovite; Sm= smectite, (Toulkeridis *et al.*, 1999).

The Na₂O values are less than 1%. Na₂O and TiO₂ values are depleted; however, both of the Fe₂O₃ and MgO values are enriched (Table 2). Many of the Fairview rocks are similar to the post-Archaeon average Australian shale (PAAS), but part of them are rich in Fe₂O₃ (Figure 3).

Ore Mineralogy

A total of 638 points were analyzed by EMPA (Table 3) on a hundred different grains of eight samples representing part of the selected samples from the Fairview Mine. This was confirmed by using LA-ICP-MS analysis; sixty-eight points were analyzed using this technique.

A number of elements have been reported such as: S, As, Fe, Mn, Cu, Co, Ni, Pb, Zn, Hg, Sb, Au, Ag, Cd, Pd, and Bi, which represent the essential and secondary chemical compositions of the ore minerals in the Fairview Mine rocks. These are pyrite, arsenopyrite, pyrrhotite, sphalerite, which contains Au 0.12wt % and Bi 0.54wt %, chalcopyrite, gersdorffite, loellingite, nickeline, and native gold. Quartz, zircon, apatite, and chromite are the significant accessory phases in the Fairview Mine ores besides the silicates.

Table 3. Selected EMPA analyses of Sulphides from the Fairview Mine

Mineral	S wt%	Fe wt%	As wt%	Co wt%	Ni wt%	Cu wt%	Zn wt%	Pd wt%	Ag wt%	Cd wt%	Sb wt%	Au wt%	Hg wt%	Pb wt%	Bi wt%	Mn wt%
pyrite-rim	52.66	46.59	0.38	-	0.1039	-	0.0105	-	-	-	-	0.031	0.0559	-	-	0.0076
pyrite-rim	52.29	46.24	1.06	-	0.2868	-	0.0217	-	0.0347	0.0802	-	-	0.0252	-	0.1522	0.0025
pyrite-rim	52.60	46.46	0.87	0.1057	0.2114	0.0734	-	0.0977	-	-	-	0.0277	0.045	-	0.3524	0.0203
pyrite-core	52.88	46.92	0.26	0.2154	0.0095	0.0695	0.0054	0.1125	-	0.042	-	-	0.0288	-	0.1737	-
pyrite-core	51.88	46.05	0.98	-	0.1179	0.0579	0.0148	-	-	0.0573	-	-	0.1026	-	-	-
pyrite-core	52.79	46.91	0.44	-	0.084	0.0977	-	0.0075	-	-	-	-	0.0721	-	-	-
pyrite-core	52.72	46.78	0.00	0.2823	0.0517	0.0529	0.001	0.0037	-	-	-	-	0.1316	-	0.1422	-
pyrite-core	50.74	46.11	2.61	-	0.1007	0.059	0.0105	0.0075	0.0484	0.0152	-	0.0033	0.0287	-	-	-
arsenopyrite	22.18	35.59	42.69	-	0.3076	0.0355	-	-	0.0744	-	-	0.024	-	-	0.3389	0.0066
arsenopyrite	21.96	35.69	42.37	-	0.0623	0.0217	-	-	0.0032	0.0676	-	0.297	0.0248	0.014	0.1723	0.0056
arsenopyrite	21.11	35.01	42.76	-	0.181	0.0175	-	-	0.0387	0.1065	-	0.0135	0.1519	-	0.3047	0.0253
arsenopyrite	21.67	34.17	43.98	-	-	0.0008	-	-	0.013	-	-	0.012	0.0594	0.1814	0.498	0.015
pyrrhotite	38.44	58.74	0.00	-	0.71	0.02	0.02	0.04	-	-	-	-	0.03	-	0.15	0.01
pyrrhotite	38.99	60.24	0.00	-	0.6	0.01	-	-	0.02	-	-	0.13	0.21	-	-	-
pyrrhotite	39.20	57.12	0.08	-	0.39	0.01	-	0.01	-	-	-	0.04	-	-	0.11	-
pyrrhotite	38.75	60.07	0.00	-	0.59	0.03	-	-	-	-	-	-	0.05	-	0.18	-
chalcopyrite	34.68	29.27	0.00	-	-	34.75	-	-	-	-	-	-	0.04	-	0.12	0.02
chalcopyrite	34.72	29.60	0.00	-	0.02	34.32	-	-	-	-	-	0.13	-	-	-	-
chalcopyrite	34.53	29.80	0.00	-	0.01	34	-	0.03	-	0.02	-	-	0.08	-	0.05	0.03
chalcopyrite	34.73	31.73	0.00	-	0.02	32.5	-	0.06	0.05	0.11	-	-	-	-	-	-
chalcopyrite	34.87	29.61	0.00	-	-	34.05	-	-	0.01	-	-	-	-	-	-	0.02
sphalerite	21.06	34.10	0.00	0.02	-	0.02	44.37	-	0.03	-	-	-	-	-	0.41	-
sphalerite	20.36	33.24	0.05	0.11	0.41	-	45.14	0.06	-	0.1	-	0.04	-	-	0.25	0.01
sphalerite	20.23	33.63	0.02	0.07	-	0.01	44.71	-	-	0.04	-	-	0.09	-	0.13	0.01
Loellingite	2.11	20.69	70.47	0.22	6.57	-	-	0.04	0.11	0.03	-	0.01	-	-	0.42	-
Loellingite	1.82	20.74	70.55	0.22	6.73	0.02	-	0.02	-	-	-	0.02	-	0.02	0.19	0.04
Loellingite	1.78	21.02	69.86	0.19	6.58	-	-	0.03	-	0.05	-	-	-	0.04	0.6	0.01

Table 4. Presentative LA-ICP-MS Analyses of the Fairview Mine's Ore Minerals (in counts per second)

Mineral	S	As	Fe	Co	Ni	Cu	Zn	Ag	Mn	Sb	Au	Hg	Pb	Bi
pyrite-rim	1444011	164332	199839900	1890	4401	1110	4037	110	8115	1193	117	125228	537	67
pyrite-rim	1191875	182713	164553900	57708	75971	6027	15129	160	61340	7009	350	120513	20736	150
pyrite-rim	1562788	150180	196304000	24638	29033	2290	-	-	-	5132	140	134053	4004	-
pyrite-rim	1100101	26160	182764379	44357	85504	8442	-	-	-	-	15969	-	52603	-
pyrite-core	1208056	428126	34902700	6071	21537	693	167	-	-	2964	263	-	3035	440
pyrite-core	1425897	495073	205062390	3945	21167	8933	-	-	-	2464	1539	-	1727	297
pyrite-core	1200404	70640	156119790	34027	117843	287	47	-	-	133	-	-	733	157
pyrite-core	361156	2162	80019279	-	187394	9205	-	-	-	-	-	-	-	-
arsenopyrite 1	337906	22036732	77666869	729850	586444	40	-	-	-	4103	73	-	-	-
arsenopyrite 1	354612	20098152	81056699	802339	604247	-	-	-	-	4869	-	-	0	-
arsenopyrite 1	361668	21708762	81857739	828065	562932	1605	-	-	-	6587	80	-	3414	-
arsenopyrite 1	399470	17591762	90167339	687229	145163	-	-	-	-	-	-	-	-	-
arsenopyrite 2	549463	24094480	117445400	15071	45783	3212	3787	811	6158	30566	215714	117426	2607	353
arsenopyrite 2	613111	26857760	109595400	687	4978	1123	-	-	-	91221	135076	118249	470	-
arsenopyrite 2	518310	22972390	102338000	6754	21254	18123	-	-	-	20214	410406	117120	293	-
arsenopyrite 2	458472	22016840	105573208	4878	48716	14240	-	-	193	48654	6217	119202	3644	-
chalcopyrite	324969	4231	32105450	143	623	23341300	5861	1060	35441	427	107	118226	2540	77
chalcopyrite	258156	927	42177269	-	20043	10433476	-	-	-	-	-	-	-	-
chalcopyrite	288864	4021	29120550	120	597	19389860	5731	787	6111	277	123	122339	1330	40
pyrrhotite	336959	5627	85247610	18602	11095	17	-	-	1505	-	3	-	157	-
pyrrhotite	314656	3969	83339760	18130	10774	177	-	-	114760	3	-	-	157	23
pyrrhotite	339858	1374	84891168	11614	7333	123	-	-	434	-	-	-	267	27
pyrrhotite	411901	901	87090318	13090	8041	170	-	10	1913	13	30	-	67	27

Gold

Native gold is present with variable amounts in part of the Fairview Mine lithologies. Gold grain sizes vary from microns for the inclusions within the sulphides (<10 μm to 30 μm) to large free-nuggets (>100 μm) in the silicates (quartz). Gold is also found submicroscopically inside sulphide structures, especially in arsenopyrite.

The LA-ICP-MS results reveal that arsenopyrite contains the highest content of invisible gold (Table 4), followed by pyrite and chalcopyrite. However, the EMPA results show no systematic relationship between gold and arsenic in pyrite (Figure 5a). Gold rather increases with high iron and sulphur content in the arsenian pyrite and arsenopyrite (Figure 6). Gold, in pyrite, formed

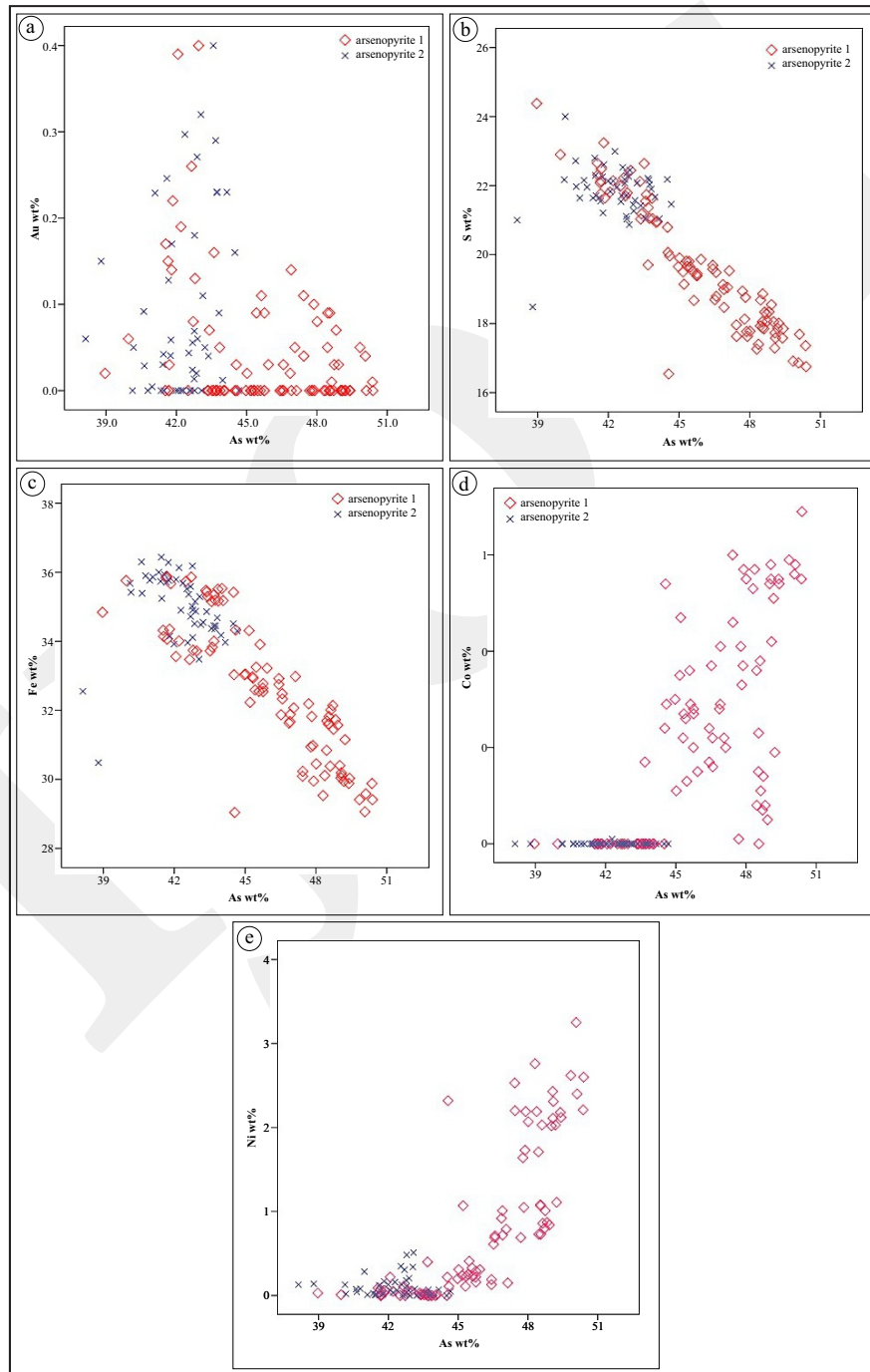


Figure 5. Relationships of major and trace elements in different arsenopyrite types from the Fairview Mine, based on EMPA.

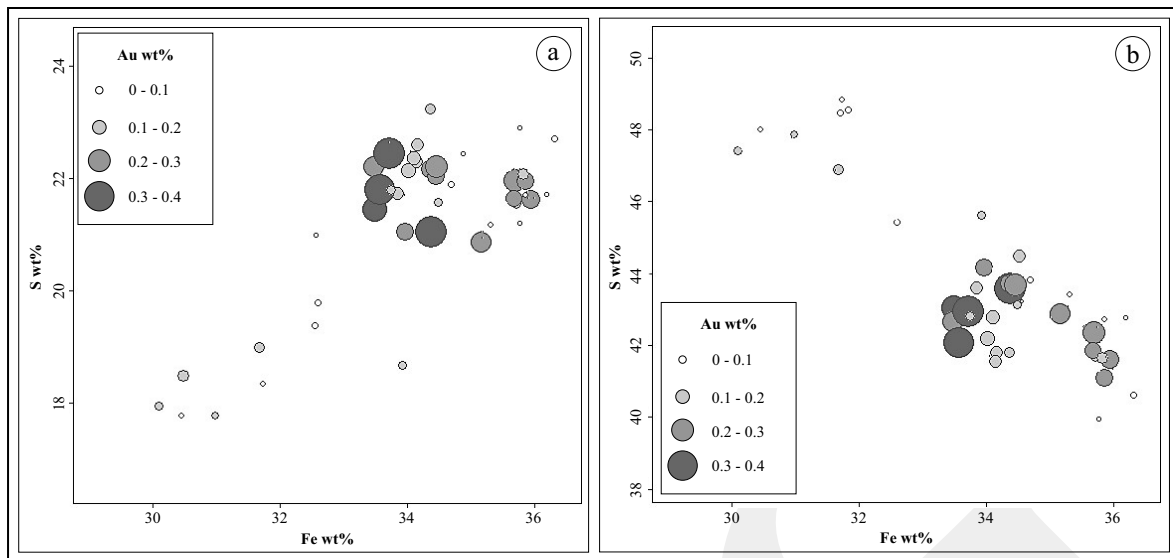


Figure 6. EMPA data of arsenopyrite from the Fairview Mine, reflecting that Au incorporates in the arsenopyrite structure due to Fe contents. EMPA data of arsenopyrite and arsenic-rich pyrite from the Fairview Mine, reflecting that Au increases in these minerals with Fe elevated contents. (a). Arsenopyrite; (b). Arsenian pyrite.

as very discrete electron at nano-scale phases (Figure 7). It shows most of the analyses locate above the solubility dashed-line.

Pyrite

Pyrite is the most dominant sulphide mineral in the earth crust, and it is found in different geological environments (Barrie *et al.*, 2011; Zhao *et al.*, 2011; Qian *et al.*, 2013). The pyrite of the Fairview

Mine is classified into two types depending on their petrography, chemistry, and associations.

The old one is (referred in some places here as core) highly porous and in deformed phase (pyrite 1). This type is situated at the cores of the pyrite grains. Pyrite 1 forms numerous textural types such as rounded, boudinage structures, and radial zoning. This type is foliated concordantly with the bedding planes of the host country

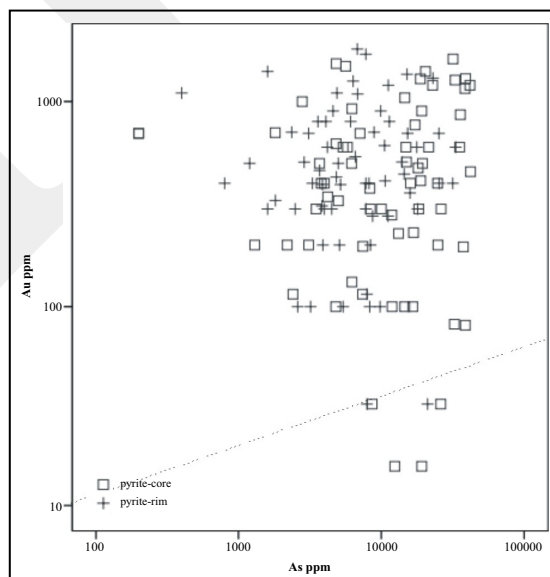


Figure 7. Au versus As plot. The solubility limit for Au in pyrite (Reich *et al.*, 2005) is shown as a dashed-line. Below this line, Au occurs in the crystal lattice of pyrite, whereas above, a component of Au is present as inclusions (Au^0). Data obtained from EMPA.

rocks, suggesting a syn-tectonic formation (Kakegawa and Ohmoto, 1999). The replacement textures are very common in this pyrite type. Recent studies on deformed pyrite exposed an elastic deformation could operate on the pyrite at 425° C (Barrie *et al.*, 2011). In addition, folded chalcopyrite grains are found deformed inside this pyrite type.

Some of these pyrite grains contain high arsenic contents (Table 4), which is very common in the orogenic gold deposits worldwide (Qian *et al.*, 2013). Pyrite type 1 contains a number of elements that are shown in Table 3. Pyrite 1 associates and contains a number of other sulphide inclusions such as pyrrhotite, chalcopyrite, arsenopyrite type 1, as well as native gold. Tiny gold grains and films commonly occur within this pyrite type; and it also contains invisible gold within its structure. These inclusions affect the analyses by mixing the results of small inclusions together. Therefore, analyzing the tiny grains (< 4µm) by EMPA is not recommended for most of the Fairview Mine rocks, and the results from these mixed analyses must be removed from the datasets before making any interpretations. These inclusions also contribute by adding values of trace elements to the chemistry of the pyrite 1 itself. No visible gold grains are found inside pyrite type 1; but it contains invisible gold.

The second type (referred in some places here as rim) is younger, compact, and well developed (pyrite 2), and grew over old pyrite type 1. Pyrite type 2 is usually found as a separate phase, but is rarely associated with arsenopyrite 2, and even less with pyrrhotite. In some cases, it is found adjacent to arsenopyrite type 2. The grain size of this type increases when located close to the late quartz-carbonate veins. Type 2 pyrite rarely contains any other sulphide inclusions; however, its mineral chemistry is characterized by lower Hg contents (Table 3). LA-ICP-MS data display a tendency for higher contents of As, Ni, Co, Au, and Hg in the pyrite type 1 than the pyrite type 2 (Table 4). Au could probably incorporate into arsenian pyrite by absorption of the Fairview pyrite and other mineral surfaces during its crystal

growth phase (Mikhlin *et al.*, 2011). Therefore, pyrite type 1 contains more gold than pyrite 2.

The LA-ICP-MS results indicate that arsenian pyrite and arsenopyrite are the most common sulphides containing invisible gold, and it is also found within the micro shears and fractures of these minerals (Cook *et al.*, 2009a). However, the amount of gold in both arsenian pyrite and arsenopyrite is very small. This is due to the nature of orogenic gold deposit of the Barberton Greenstone Belt, in which long-term remobilization and recrystallization process (Cook *et al.*, 2009a, b) subjected sulphides.

Arsenopyrite

The arsenic-rich minerals of the Fairview Mine are represented by arsenopyrite and nickel-rich loellingite, in which the Ni content reaches up to 12 wt. % (Table 3). Arsenopyrite shows different sizes and shapes. It forms euhedral crystals, irregular aggregates, and laths, which reflect variable formation conditions. The arsenopyrite of this mine can be classified into two types which vary in their morphology, trace elements contents, and mineral associations.

Arsenopyrite type 1: This type forms irregular grain shapes, occasionally sub-rounded, and is usually associated with pyrrhotite, chalcopyrite, and minor pyrite. It contains both visible and invisible gold. This arsenopyrite forms many textures, and usually shows mimetic twin lamellae. This is due to their heterogeneous origin (Ramdohr, 1958). EMPA results show that arsenopyrite of the Fairview Mine has Au, Ag, Sb, Bi, Ni, Hg, and Co values higher than that of pyrite (Table 3). Gold content in this type of arsenopyrite increases with high values of iron and sulphur, due to the substitution of Fe by Au (Cabri *et al.*, 2000). Zoning is often present in this arsenopyrite type, which suggests variation in the element distribution and chemical alteration or metasomatism remobilization that has affected these ores. This arsenopyrite type contains higher Au and Hg than arsenopyrite type 2 (Figure 5).

Arsenopyrite type 2: This type forms euhedral grains and is usually associated with pyrite type

2, or occurs as individual crystals within the silicates. In some samples, this arsenopyrite is found in disseminated patches with small amounts of pyrite type 2 grains. This generation contains small native gold grains situated in fractures and fissures. This type of arsenopyrite is infrequently found in a circular pattern.

Generally, gold values in arsenopyrite increase with higher values of sulphur and iron rather than arsenic (Figure 6). This is due to the substitution of Fe by Au in arsenopyrite (Cabri *et al.*, 2000), which contradict with many researches that say gold participates in the arsenic-rich pyrite composition due to arsenic contents (Mikhlin *et al.*, 2011).

Chalcopyrite and Pyrrhotite

Chalcopyrite is often associated with arsenopyrite type 1, pyrrhotite, and less with pyrite type 1. It formed an intergrowth with pyrrhotite, suggesting a contemporaneously formation. Chalcopyrite is usually found as aggregates and fracture fillings. However, it formed euhedral bi-pyramidal crystals found inside pyrrhotite grain. Chalcopyrite in this mine is found forming kinked bands inside the pyrite type 1.

Chalcopyrite contains up to 0.21 wt. % As, 0.03 wt. % Ni, 0.014 wt. % Pd, 0.04 wt. % Cd, 0.18 wt. % Au, 0.18 wt. % Hg, and 0.13 wt. % Bi. The LA-ICP-MS analyses indicate that chalcopyrite of the Fairview Mine contains chemically bounded gold (Table 4).

Pyrrhotite is dominant in the Fairview Mine rocks, displaying stock-work textural texture and patch-like aggregates, usually occurring in anhedral crystal shapes in the matrix. Based on EMPA data, pyrrhotite contains As 0.7 wt. %, Ni 0.7 wt. %, Pd 0.1 wt. %, Cu 0.2 wt. %, Au 0.15 wt. %, and Hg 0.3 wt. %. The iron contents in the pyrrhotite are variable (Table 3).

This pyrrhotite encloses tiny grains of either cobaltian pentlandite or (Co, Ni)-rich arsenopyrite. Pyrrhotite is also associated with nickel-sulphides (Guerra and Shepherd, 2011), especially gersdorffite. Obviously, the (Ni and Co) contents and other trace elements bounce the pyrrhotite to

be more economically valuable. The pyrrhotite matrix commonly displays symptomatic textures of mechanical stress and deformation, such as disaggregation and lenticular zoning.

Gersdorffite and Loellingite

These minerals represent the Ni-rich arsenides in the Fairview Mine: Gersdorffite contains Co 4.0 wt. %, Bi 0.8 wt. %, Ag 0.45 wt. %, Au 1.5 wt. %, Hg 0.15 wt.%, Pb 0.15 wt. %, Cd 0.17 wt. %, and small amounts of Fe. In gersdorffite, Fe and Co affect the contents of As, S, and Ni. Loellingite contains up to Ni 11.6 wt. %, Co 6.6 wt. %, Bi 0.4 wt. %, Ag 0.1 wt. %, Pb 0.2 wt. %, and S 2.1 wt. %. The cobalt contents increase with iron and sulphur, and have reverse relation with nickel. As/S ratio decreases with the increase in Fe.

The antimony content in these arsenide phases reaches up to 0.12 wt. %. These minerals forming euhedral crystals, are found as inclusions close to the pyrite type 2 and arsenopyrite type 2. Gold content in Ni-rich arsenides of the Fairview Mine is higher than in pyrite, arsenopyrite, and pyrrhotite. Generally, in the Fairview Mine, the arsenic of later hydrothermal solutions replaced sulphur. At the same time, significant amounts of Ni-Co replaced Fe in the old pyrite type and pyrrhotite to form these Ni and Co-rich sulphides and sulfosalts. The contents of nickel in the gersdorffite depend on the values of arsenic, and it correlates negatively with cobalt content. The iron content increases with the access of sulphur and cobalt. There was no pentlandite observed within the Fairview Mine sulphides. This is because of nickel partitioning into nickeline (the average: Ni= 30.4wt. %, As= 60wt. %, Fe=7.8wt. %, and Sb = 0.08wt. %), gersdorffite, and loellingite that contains nickel up to 11.55 wt. % and Co 6.58 wt. %.

DISCUSSIONS

Pyrite

In this mine, bands of pyrite and arsenopyrite are common (Figure 8a), indicating repetition of

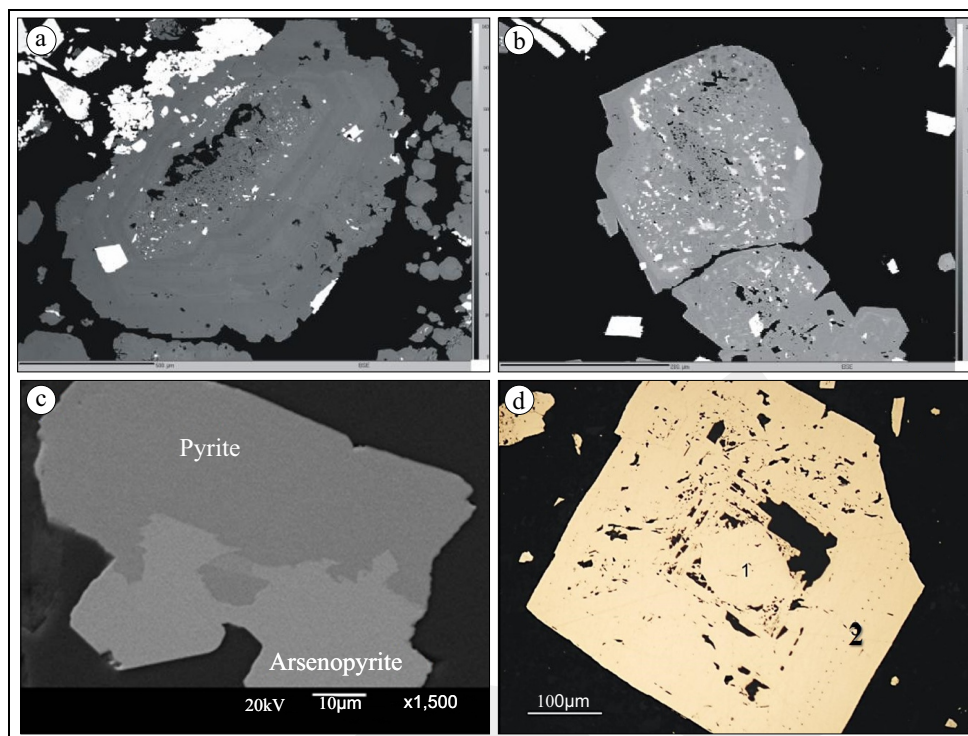


Figure 8. Photomicrographs of: (a). backscattered image shows growth banding between arsenopyrite and pyrite; (b). porous pyrite type 1 involves tiny arsenopyrite inclusions; (c). Ex-solution and reaction rims between pyrite and arsenopyrite suggest later reaction of As-rich solution with pyrite; d. Rounded (possibly detrital) pyrite overgrown by pyrite 2.

depositional cycles or chemical zoning (Hu *et al.*, 2006; Altigani *et al.*, 2016). Infrequently, pyrite bands alternate with quartz-carbonate layers, which is consistent with the proposed concepts of strata bound mineralization of the Barberton Greenstone Belt (BGB) by Williams (1997).

Generally, zoning in pyrite is very common (Figure 8a), reflecting different chemical compositions of these pyrite types (Agange *et al.*, 2014; Altigani *et al.*, 2016) caused by the variability in trace element contents (Zhao *et al.*, 2011) and precipitation at different times (Hu *et al.*, 2006; Hofmann *et al.*, 2009). The pyrite of the Fairview Mine is subdivided into two types based on variations in morphology, chemistry, and mineral associations (Altigani *et al.*, 2016).

Porous pyrite type 1, which is abundant in the Fairview ores (Figure 8b), is thought to have formed as a result of transformation of iron oxides into pyrite with increasing sulphur fugacity (Qian *et al.*, 2010). The pores in this pyrite type might be formed during formation, metamorphic growth, or during recrystallization. Ex-solution is a com-

mon feature between nickeliferous arsenides and nickeliferous pyrite, which contains up to 3.9% Ni (Figure 8c).

The results of EMPA revealed a negative correlation between arsenic and iron in the pyrite, indicating a substitution of iron by arsenic. LA-ICP-MS results show no systematic relationship between arsenic and gold in the pyrite of the Fairview Mine, which is due to physical incorporation of gold in pyrite rather than chemical precipitation. The differences in arsenic contents in both pyrite types reflect different incorporation processes for As during the pyrite formation (Qian *et al.*, 2013). The arsenic forms concentric growth zones in pyrite type 2, but rather forms inclusions in pyrite type 1. Rounded pyrite may represent the earliest generation in this mine, because it is found surrounded by types 1 and 2 of pyrite (Figure 8d). This rounded pyrite of the Fairview Mine could have derived from different sources, which might be one of the followings: (1) Sulphides of magmatic, magmatic-hydrothermal or metamorphism related to hydrothermal origin,

hosted in granitoid-greenstone terrains, (2) Pre-existence of sedimentary rock successions, or (3) Syn-depositional to diagenetic intraformational sulphides representing primary chemical precipitates, early diagenetic products, or secondary replacements (Hofmann *et al.*, 2009).

Rouchon *et al.* (2009) analyzed detrital pyrite from the Hooggenoeg Formation of the BGB, and found that it contains various copper amounts (up to 1.7 wt. %) and traces of Pb (0.1 - 0.5 wt. %), As (0.05 - 0.2 wt. %), Zn (200 - 300 ppm), Co (100 - 150 ppm), Sb (100 ppm), Cd (30 - 50 ppm), and Cr (10 - 30 ppm). They also observed that diagenetic pyrite has higher Cu (up to 1.1 wt.%) and Co (up to 2.6 wt.%), and lower As, Pb, Ni, Zn, Cd, Co, Cr, and Sb contents than detrital pyrite. In this study, the pyrite type 2 is comparable with Rouchon *et al.* (2009) observations. It contains As up to 2.1 wt. %, Co 0.23 wt. %, Cu 0.1 wt. %, Pb 0.1 wt. %, Hg 0.2 wt. %. Elements like Ni, Co, and Ag increase with the elevated levels of arsenic in the pyrite, which was also observed by Maddox *et al.* (1998). Gold contents increase with the high Ni values; it reaches up to 1.13 wt. % in the arsenic-rich zones of pyrite (see also Reich *et al.*, 2005; Cook *et al.*, 2009a). High Ni contents in pyrite may indicate a mafic or ultramafic provenance of the ore-forming fluid (Zhao *et al.*, 2011).

Pyrite of the Fairview Mine contains submicroscopic inclusions of rutile and chrome-rich

magnetite. The presence of chrome-rich magnetite in pyrite indicates mafic to ultramafic associations, such as the komatiite-hosted sulphide deposits at Kambalda in Western Australia (Dare *et al.*, 2012). Stiegler *et al.* (2010) noted that there were no significant criteria for metasomatism modification affected these chrome-rich magnetite grains.

Pyrrhotite and Chalcopyrite

Anhedral microstructures are commonly observed in pyrrhotite and chalcopyrite of this mine, as well as coarsening at the hinges of the host rock micro-folds (Figure 9a), which suggests syn-tectonic formation of chalcopyrite (Barrie *et al.*, 2007). Chalcopyrite forms zoned and gradational rims with pyrrhotite, indicating growth zones, or repeated fluid cycles. This possibly shows that chalcopyrite is formed due to replacement of the pyrrhotite in the presence of aqueous copper (Elliott and Watling, 2011). The morphology of the chalcopyrite in this mine suggests the presence of two generations or depositional episodes (massive and euhedral).

Pyrrhotite of the Fairview Mine has high iron content, which suggests formation in a low-sulphur and/or low-temperature environment (low-grade metamorphism). Infrequently, some remnants of fine-grained pyrrhotite are situated inside, or are overgrown by arsenopyrite type 2. This implies fluctuations of the arsenic contents in different stages of hydrothermal solutions (Figure 9b).

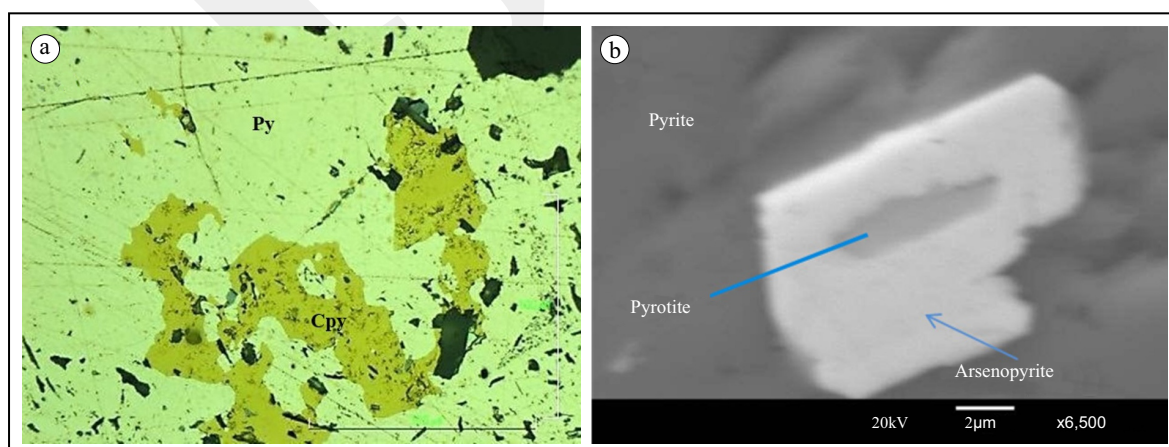


Figure 9. Photomicrographs of: (a). Kinked chalcopyrite inside pyrite; (b). Inclusion of pyrrhotite inside arsenopyrite, and both are enclosed by pyrite.

Gold

Two gold generations (types) have been observed (Figure 10a). The first one is associated with sulphides (mainly pyrite, arsenian-pyrite, arsenopyrite, pyrrhotite, and chalcopyrite), indicating one or more of these assumptions: (1) Early existence of gold grains which were overgrown or formed simultaneously with pyrite, (2) Co-precipitation of gold in the structures of these sulphides, suggesting direct contribution of the ore-forming hydrothermal system rather than recrystallization effects (Economou-Eliopoulos *et al.*, 2007), or (3) Later auriferous hydrothermal fluids that deposited gold in fractured surface of the pyrite.

The second gold generation is found as free lodes (Figure 10b), filling the spaces between silicates. Gold can be adsorbed on the surface of silicate (especially quartz and alkali-feldspar), and gold particles can grow to form aggregates and nuggets (Mohammadnejad *et al.*, 2012). The sulphides present in the assemblage of free gold are arsenopyrite and pyrrhotite rather than pyrite in most of the samples. This gold generation could reflect metamorphic remobilization and distribution of the pre-existent gold grains (type 1) (Vaughan and Kyin, 2004; Ciobanu *et al.*, 2009).

No systematic relationship has been observed between gold and arsenic in pyrite during this study and in other gold deposits worldwide (Cook and Chryssoulis 1990; Fleet *et al.*, 1993; Zachariáš *et al.*, 2004; Sung *et al.*, 2009; Bi *et al.*,

2011). Occasionally, gold can be found related to tellurium rather than arsenic, but even this relationship does not exist.

God and Zemann (2000) and Mikhlin *et al.* (2011) summarized the process of gold incorporation in pyrite due to arsenic traces. The observed nonsystematic gold-arsenic relationship is probably caused by the heterogeneity and differences in the elemental distributions in the pyrite grains (Winderbaum *et al.*, 2012; Altigani *et al.*, 2016). This kind of heterogeneity leads to uncertain or nonlinear overall relationships between Au and As. Therefore, the correlation between these two elements could be only valid in more homogenous grains, and it implies physical precipitation of gold in pyrite rather than chemical reaction processes.

Gold values in both pyrite types are low, which is consistent with other orogeny-type gold deposits worldwide (Zhao *et al.*, 2011). LA-ICP-MS smooth depth profiles on pyrite revealed that gold and silver occurred in discrete grains in the pyrite type 1, which might reflect coexistence formation (Cook *et al.*, 2009b; Sung *et al.*, 2009; Bi *et al.*, 2011) of native gold and the pyrite.

Mineralization Style

The quartz-reef deposits in the Barberton Greenstone Belt are probably compared to that of the Kalgoorlie Belt in the Western Australia. In which, the gold was thought to be transported as reduced sulphur species, in low salinity meta-

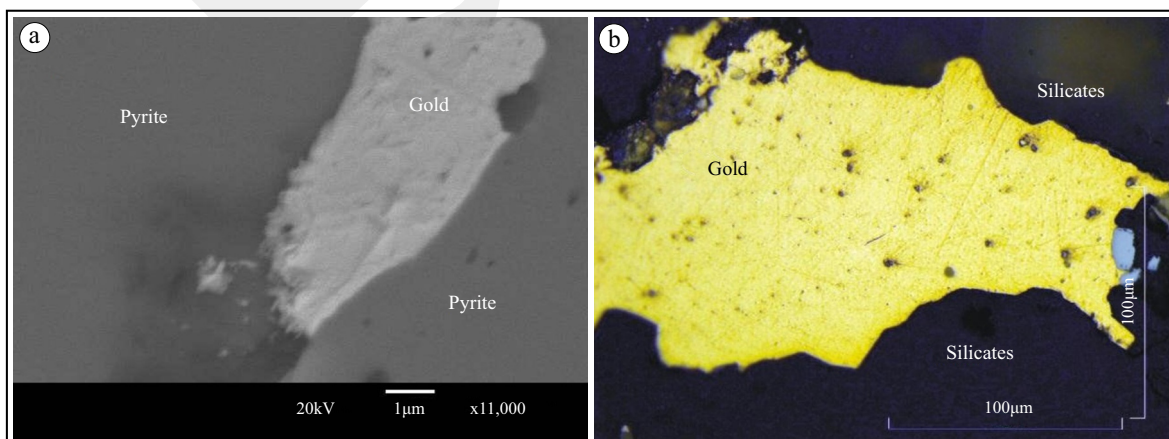


Figure 10. Photomicrographs of: (a). Tiny gold grain contained by pyrite; (b). Free-lode gold grain in silicate matrix.

morphic fluids rich in H₂O and CO₂ and ± CH₄ (Hammond *et al.*, 2007). Gold is deposited due to the reaction of sulphur with the iron in the host rocks (sea-bed/possibly mafic or ultramafic?) to form pyrite and other iron-containing sulphides (Qian *et al.*, 2010). This explains the affinity of gold towards iron and sulphur rather than arsenic in arsenopyrite. In arsenopyrite, the gold values increase with high values of sulphur and iron rather than arsenic (Cabri *et al.*, 2000), which is contradictory with many researches who mentioned that gold participates in the pyrite composition was due to arsenic traces (*e.g.* Mikhlin *et al.*, 2011).

Dehydration (dewatering) due to later metamorphism processes of clastic metasedimentary rocks in greenstone belts has been recognized as significant source generated fluids, causing intensive metasomatism and ore depositions in the mafic and/or ultramafic metavolcanics (Saha and Venkatesh, 2002; Dziggel *et al.*, 2007; Ordonez-Calderon *et al.*, 2008).

Most of gold deposits in the BGB are located in the second and third order structures (Dirks *et al.*, 2013), or in the fault intersections corresponding to places of low stress which increase fluid intake and location. Gold in Fairview Mine is normally attached to quartz-carbonate reefs; the mineralized fractures are spatially proximal to large-scale compressional and/or transpressional shear zone across the Kaapvaal Craton (Dziggel *et al.*, 2007 and 2010). The Au-mineralized fluids are usually characterized by the range of P-T conditions of ca. 200 - 650° C and 1 - 5 kbar, with low salinity and CO₂-rich. These fluids were generated from metamorphic devolatilization and metamorphic reactions in the middle and lower crust (Dziggel *et al.*, 2007).

The dominant sulphides in the Fairview Mine are pyrite, arsenopyrite, and pyrrotite, besides Ni-rich arsenides and sulfosalts. This assemblage is similar to that of the mesothermal gold ores in the Archaean Yilgarn Craton of Western Australia described by Vaughan and Kyin (2004).

The source of the fluids, which precipitated these sulphides, is uncertain. Firstly, it might be

originated from residual magmatic fluids that segregated after the formation of the Barberton Greenstone Belt ores and migrated upward through the greenstones during the early stages of brittle deformation (dip and strike-slip shear zones). Another source could be due to the metasomatism associated with shearing that could represent the continued influence, which moved these fluids as it evolved. A third possibility is that it could have occurred during a separate episode linked to the dehydration associated with the metamorphism of the mafic/ultramafic rocks (komatiite?).

The mineralization of this mine is syn-to late tectonic and postdates the peak of metamorphism. The relatively high formation temperatures of gold deposits reflect an orogenic (mesothermal) type which is also confirmed by the low gold content in pyrite due to sulphide recrystallization and remobilization during regional metamorphic overprinting, which is consistent with many other orogenic-type gold deposits world-wide (Zhao *et al.*, 2011).

The structural pattern of gold mineralization in this mine is quite similar to that of the Pilbara in Western Australia (Thèbaud *et al.*, 2008). The main host rocks of gold mineralization in this mine belong to the Fig Tree and the Moodies Group sedimentary rocks (Dziggel *et al.*, 2007).

The mineralogical, chemical feature, and relationships suggest at least two generations or types of mineralization at the Fairview Mine. This may be due to two separate mineralization events which occurred in different times, or as a consequence of remobilization and redistributions of old (parent) gold-bearing sulphide deposits.

CONCLUSIONS

The Fairview Gold Mine, lithologically consists of greywackes, metapelites, and arkoses. These rocks have geochemical calc-alkaline affinities, suggesting a deposition in back-arc basins. These rocks mainly consist of (up to 67 wt. % quartz, up to 40 wt. % micas), and minor

dolomite, amphiboles, and chlorite, suggesting low metamorphic facies.

In these rocks, four generations of quartz vary in their textures and shapes. The ancient primary depositional structures, such as trough-cross bedding and lamination, are still conserved which prove the low-grade metamorphic green schist facies for the Fairview lithology. All lithology units (metapelites, greywackes, and lesser in arkoses) of the Fairview Mine host pyrite, arsenopyrite, pyrrhotite, chalcopyrite, loellingite, nickeline, gersdorffite, and rarely sphalerite, besides the gold. Ex-solution and lateral zoning are the common microtextures in these sulphides, especially in pyrite and arsenopyrite, which indicate a repetition of depositional cycles, or presolid-state chemical reactions. Most of these sulphides contains gold in chemical and mineralogical forms.

The pyrite of the Fairview Mine is classified into at least two types; the old, highly porous and in deformed phase (pyrite 1), and the late one well-developed (pyrite 2). In some of the Fairview samples, the pyrite 1 is situated in the core of the pyrite grains, sometimes as detrital, while the later pyrite found in the rims. This, besides the variations in arsenic, and probably (Ni, Co) contents, formed zoning textures between both of the pyrite types. LA-ICP-MS data of the Fairview pyrite display an increase in Ni, Co, Hg, Bi, Ag, and Au contents with the high levels of arsenic. However, Au replaces Fe in arsenopyrite lattice.

The LA-ICP-MS results show that arsenic-rich pyrite is the most gold-containing mineral as elemental and mineralogical phases, then arsenopyrite and chalcopyrite. Au was probably incorporated into arsenian pyrite by adsorbing on the pyrite and other mineral surfaces during its crystal growth; this causes pyrite 2 contain more gold rather than pyrite 1.

Native gold is present in various amounts in the whole of the Fairview Mine rocks. Gold is associated with Ni-rich arsenides and gersdorffite. The gold grain size is also varying from microns for the inclusions within the sulphides (<10 µm to 30 µm) to large free-nuggets (>100 µm) in the silicates. The results obtained from this research

revealed that Fairview Mine ore deposits were possibly classified into two groups differ in their chemical, mineralogical, and associations.

ACKNOWLEDGEMENTS

Deep thanks go to the Geology Department at the University of Pretoria for providing the laboratories and instruments for XRD, XRF, and EMPA analyses of the samples in this research. Special appreciation goes to Prof. R.K.W. Merkle for his valuable comments, revisions, and suggestion. Thanks extended to the South African Police Forensic Labs in Pretoria that provide the studied samples and for allowing us to use the LA-ICP-MS.

REFERENCES

- Agange, A., Hofmann, A., and Przybyłowicz, W., 2014. Trace element zoning of sulfides and quartz at Sheba and Fairview gold mines: clues to Mesoarchean mineralization in the Barberton Greenstone Belt, South Africa. *Ore Geology Review*, 56, p.94-114. DOI: 10.1016/j.oregeorev.2013.08.016
- Altigani, M.A.H., Merkle, R.K.W., and Dixon R.D., 2016. Geochemical identification of episodes of gold mineralization in the Barberton Greenstone Belt, South Africa, *Ore Geology Reviews*, 75, p.186-205. DOI: 10.1016/j.oregeorev.2015.12.016
- Barrie, C.D., Boyle, A.P., and Prior, D.J., 2007. An analysis of the microtextures developed in experimentally deformed polycrystalline pyrite and minor sulphide phases using electron backscatter diffraction. *Journal of Structural Geology*, 29, p.1494-1511. DOI: 10.1016/j.jsg.2007.05.005
- Barrie, C.D., Pearce, M.A., and Boyle, A.P., 2011. Reconstructing the pyrite deformation mechanism map. *Ore Geology Reviews*, 39 (4), p.265-276. DOI: 10.1016/j.oregeorev.2011.03.006

- Bi, S., Li, J., Zhou, M., and Zhan, L., 2011. Gold distribution in As-deficient pyrite and telluride mineralogy of the Yangzhaiyu gold deposit, Xiaoqinling district, southern North China craton. *Mineral Deposita*, 46, p.925-941. DOI: 10.1007/s00126-011-0359-2
- Bliss, J.D., 1992. *Developments in ore deposit modelling*. In: Bulletin. USGS, Denver, 2004 168pp.
- Brandl, G., Cloete, M., and Anhaeusser, C.R., 2006. Archaean greenstone belts. In: Johnson, M.R., Anhaeusser, C.R., and Thomas, R.J. (eds.), *Geology of South Africa*, Geological Society of South Africa, Johannesburg/ Council for Geosciences, Pretoria, p.9-56.
- Bumby, A.J., Eriksson, P.G., Catuneanu, O., Nelson, D.R., and Rigby, M.J., 2011. Meso-Archaean And Palaeo-Proterozoic Sedimentary Sequence Stratigraphy of The Kaapvaal Craton. *Marine and Petroleum Geology*, 33 (1), p.92-116. DOI: 10.1016/j.marpetgeo.2011.09.010
- Cabri, L.J., Newville, M., Gordon, R.A., Crozier, E.D., Sutton, S.R., McMahon, G., and Jiang, D.T., 2000. Chemical speciation of gold in arsenopyrite. *The Canadian Mineralogist*, 38 (5), p.1265-1281. DOI: 10.2113/gscanmin.38.5.1265
- Chen, Z., 1999. Inter-element fractionation and correction in laser ablation inductively coupled plasma mass spectrometry. *Journal of Analytical Atomic Spectrometry*, 14, p.1823-1828. DOI: 10.1039/A903272J
- Ciobanu, C.L., Cook, N.J., Pring, A., Brugger, J., Danyushevsky, L.V., and Shimizu, M., 2009. 'Invisible gold' in bismuth chalcogenides. *Geochimica et Cosmochimica Acta*, 73 (7), p.1970-1999. DOI: 10.1016/j.gca.2009.01.006
- Cloete, M., 1999. Aspects of volcanism and metamorphism of the Onverwacht Group lavas in the south-western portion of the Barberton greenstone belt. *Memoir of Geological Survey of South Africa*, 84, 232 pp.
- Condie, K.C., 1993. Chemical composition and evolution of the upper continental crust: contrasting results from surface samples and shales. *Chemical Geology*, 104, p.1-37. DOI: 10.1016/0009-2541(93)90140-E
- Cook, N.J. and Chryssoulis S.L., 1990. Concentrations of invisible gold in the common sulfides. *Canadian Mineralogist*, 28, p.1-16.
- Cook, N.J., Ciobanu, C.L., and Mao, J., 2009a. Textural control on gold distribution in As-free pyrite from the Dongping, Huangtuliang and Hougou gold deposits, North China Craton. *Chemical Geology*, 264 (1-4), p.101-121. DOI: 10.1016/j.chemgeo.2009.02.020
- Cook, N.J., Ciobanu, C.L., Pring, A., Skinner, W., Shimizu, M., Danyushevsky, L., Saini-Eidukat, B., and Melcher, F., 2009b. Trace and minor elements in sphalerite: A LA-ICP-MS study. *Geochimica et Cosmochimica Acta*, 73 (16), p.4761-4791. DOI: 10.1016/j.gca.2009.05.045
- Cook, N.J., Ciobanu, C.L., Danyushevsky, L.V., and Gilbert, S., 2011. Minor elements in bornite and associated Cu-(Fe)-sulfides: a LA-ICPMS study. *Geochimica et Cosmochimica Acta*, 75 (21), p.4761-4791. DOI: 10.1016/j.gca.2011.08.021
- Dare, S.A.S., Barnes, S., and Beaudoin, G., 2012. Variation in trace element content of magnetite crystallized from a fractionating sulfide liquid, Sudbury, Canada: Implications for provenance discrimination. *Geochimica et Cosmochimica Acta*, 88, p.27-50. DOI: 10.1016/j.gca.2012.04.032
- De Wit, M.J., Roering, C., Hart, R.J., Armstrong, R.A., De Ronde, C.E.J., Green, R.W.E., Tredoux, M., Peberdy, E., and Hart, R.A., 1992. Formation of an Archaean continent. *Nature*, 357, p.553-562. DOI: 10.1038/357553a0
- De Wit, M.J., Furnes, H., and Robins, B., 2011. Geology and tectono-stratigraphy of the Onverwacht Suite, Barberton Greenstone Belt, South Africa. *Precambrian Research*, 186 (1-4), p.1-27. DOI: 10.1016/j.precamres.2010.12.007
- Diener, J.F.A., Stevens, G., Kisters, A.F.M., and Poujol, M., 2005. Metamorphism and exhumation of the basal parts of the Barberton greenstone belt, South Africa: constraining

- the rates of Mesoarchaeon tectonism. *Precambrian Research*, 143 (1-4), p.87-112. DOI: 10.1016/j.precamres.2005.10.001
- Dirks, P.H.G.M., Charlesworth, E.G., Munyai, M.R., and Wormald, R., 2013. Stress analysis, post-orogenic extension and 3.01 Ga gold mineralization in the Barberton Greenstone Belt, South Africa. *Precambrian Research*, 226, p.157-184. DOI: 10.1016/j.precamres.2012.12.007
- Dziggel, A., Otto, A., Kisters, A.F.M., and Meyer, F.M., 2007. Tectono metamorphic controls on Archaean gold mineralization in the Barberton greenstone belt, South Africa: an example from the New Consort gold mine. In: Van Kranendonk, M., Smithies, R.H., and Bennett, V. (eds.), *Earth's Oldest Rocks. Developments in Precambrian Geology*, 15, p.699-727. DOI: 10.1016/S0166-2635(07)15058-1
- Dziggel, A., Poujol M., Otto A., Kisters, A.F.M., Trieloff, M., Schwarzd, W.H., and Meyer, F.M., 2010. New U-Pb and $^{40}\text{Ar}/^{39}\text{Ar}$ ages from the northern margin of the Barberton greenstone belt, South Africa: Implications for the formation of Mesoarchaeon gold deposits. *Precambrian Research*, 179, p.206-220. DOI: 10.1016/j.precamres.2010.03.006
- Economou-Eliopoulos, M., Eliopoulos, D.G., and Chryssoulis, S., 2007. A comparison of high-Au massive sulfide ores hosted in ophiolite complexes of the Balkan Peninsula with modern analogues: Genetic significance. *Ore Geology Reviews*, 33 (1), p.81-100. DOI: 10.1016/j.oregeorev.2006.10.009
- Elliot, A.D. and Watling, H.R., 2011. Chalcopyrite formation through the metathesis of pyrrhite with aqueous copper. *Geochimica et Cosmochimica Acta*, 72 (8), p.2103-2118. DOI: 10.1016/j.gca.2011.01.033
- Eriksson, K.A., 1978. Alluvial and destructive beach facies from the Archean Moodies Group, Barberton Mountain Land South Africa and Swaziland. *Fluvial Sedimentology. Canadian Society of Petroleum Geology, Memoir*, 5, p.287-311.
- Eriksson, K.A., Krapez, B., and Fralik, P.W., 1997. Sedimentological aspects. In: De Wit, M.J. and Ashwal, L.D. (eds.), *Greenstone Belts*. Clarendon Press, Oxford, p.33-54.
- Eriksson, P.G., Martins-Neto, M.A., Nelson, D.R., Aspler, L.B., Chiarenzelli, J.R., Catuaneanu, O., Sarkar, S., Altermann, W., and Rautenbach, W., 2001. An introduction to Precambrian basins: their characteristics and genesis. *Sedimentary Geology*, (141-142), p.1-35. DOI: 10.1016/S0037-0738(01)00066-5
- Fleet, M.E., Chryssoulis, S.L., Maclean, P.J., Davidson, R., and Weisener, G.G., 1993. Arsenian pyrite from gold deposits: Au and As distribution investigated by SIMS and EMP, and colour staining and surface oxidation by XPS and LIMS. *The Canadian Mineralogist*, 31, p.1-17.
- Frimmel, H.E., 2005. Archaean atmospheric evolution: evidence from the Witwatersrand gold fields, South Africa. *Earth-Science Reviews* 70 (1-2), p.1-46. DOI: 10.1016/j.earscirev.2004.10.003
- Furnes, H., De Wit, M.J., Robins, R., and Sandsta, N.R., 2010. Volcanic evolution of the Upper Onverwacht Suite, Barberton Greenstone Belt, South Africa. *Precambrian Research*, 186 (1-4), p. 28-50. DOI: 10.1016/j.precamres.2010.11.002
- Gaboardi, M. and Humayun, M., 2009. Elemental fractionation during LA-ICP-MS analysis of silicate glasses: implications for matrix-independent standardization. *Journal of Analytical Atomic Spectrometry*, 24, p.1188-1197. DOI: 10.1039/B900876D
- God, R. and Zemann, J., 2000. Native arsenic-realgar mineralization in marbels from Saualpe, Carinthia, Austria, *Mineralogy and Petrology*, 70, p.37-53. DOI: 10.1007/s007100070012
- Goldfarb, R.J., Groves, D.I., and Gardoll, S., 2001. Orogenic gold and geologic time: a global synthesis. *Ore Geology Reviews*, 18, p. 1-75. DOI: 10.1016/S0169-1368(01)00016-6
- Grooves, D.I. and Foster, R.P., 1991. Archean lode gold deposits. In: R.P. Foster (ed.), *Gold*

- Metallogeny and exploration*, 3, p.63-96. DOI: 10.1007/978-1-4613-0497-5_3
- Grosch, E.G., Kosler, J., McLoughlin, N., Drost, K., Slama, J., and Pedersen, R.B., 2011. Paleoproterozoic detrital zircon ages from the earliest tectonic basin in the Barberton Greenstone Belt, Kaapvaal craton, South Africa. *Precambrian Research*, 191 (1-2), p.85-99. DOI: 10.1016/j.precamres.2011.09.003
- Guerra, E. and Shepherd, J.L., 2011. The effect of polytetrafluoroethylene on pressure oxidation of nickeliferous pyrrhotite. *Hydrometallurgy*, 106, p.179-182. DOI: 10.1016/j.hydromet.2011.01.004
- Hammond, N.Q., Moore, J.M., and Sheets, R.W., 2007. Physico-chemical conditions of ore-forming fluids associated with genesis of the Kalahari Goldridge deposit, Kraaipan Greenstone Belt, South Africa. *Ore Geology Reviews*, 30, p.106-134. DOI: 10.1016/j.oregeorev.2005.11.003
- Hofmann, A., 2005. The geochemistry of sedimentary rocks from the Fig Tree Group, Barberton greenstone belt: Implications for tectonic, hydrothermal and surface processes during mid-Archaean times. *Precambrian Research*, 143 (1-4), p.23-49. DOI: 10.1016/j.precamres.2005.09.005
- Hofmann, A., Bekker, A., Rouxel, O., Rumble, D., and Master, S., 2009. Multiple sulphur and iron isotope composition of detrital pyrite in Archaean sedimentary rocks: A new tool for provenance analysis. *Earth and Planetary Science Letters*, 286 (3-4), p.436-445. DOI: 10.1016/j.epsl.2009.07.008
- Hu, G., Dam-Johansen, K., Wedel, S., and Hansen, J.P., 2006. Decomposition and oxidation of pyrite. *Progress in Energy and Combustion Science*, 32 (3), p.295-314. DOI: 10.1016/j.peccs.2005.11.004
- Humayun, M., Davis F.A., and Hirschmann, M.M., 2010. Major element analysis of natural silicates by laser ablation ICP-MS. *Journal of Analytical Atomic Spectrometry*, 25, p.998-1005. DOI: 10.1039/C001391A
- Kakegawa, T. and Ohmoto, H., 1999. Sulfur isotope evidence for the origin of 3.4 to 3.1 Ga pyrite at the Princeton gold mine, Barberton Greenstone Belt, South Africa. *Precambrian Research*, 96, p.209-224. DOI: 10.1016/S0301-9268(99)00006-6
- Kamo, S.L. and Davis, D.W., 1994. Reassessment of Archean crust development in the Barberton Mountain Land, South Africa, based on U-Pb dating. *Tectonics* 13, p.167-192. DOI: 10.1029/93TC02254
- Kent, L.E., 1980. Stratigraphy of South Africa. South African Committee for Stratigraphy, *Geological Survey of South Africa, Handbook*, 8, 960pp.
- Kisters, A.F.M., Belcher, R.W., Poujol, M., and Dziggel, A., 2010. Continental growth and convergence-related arc plutonism in the Mesoarchaean: Evidence from the Barberton granitoid-greenstone terrain, South Africa. *Precambrian Research*, 178, p.15-26. DOI: 10.1016/j.precamres.2010.01.002
- Kohler, E.A. and Anhaeusser, C.R., 2002. Geology and geodynamic setting of Archaean silicic metavolcaniclastic rocks of the Bien Venue Formation, Fig Tree Group, northeast Barberton greenstone belt, South Africa. *Precambrian Research*, 116, p.199-235. DOI: 10.1016/S0301-9268(02)00021-9
- Kranendonk, M.J. Van, Smithiers, R.H., and Bennet, V.C., 2007. *Earth' Oldest Rocks Developments in Precambrian Geology*, 15, 1331pp.
- Kranendonk, M.J. Van, 2011. Cool greenstone drips and the role of partial convective overturn in Barberton greenstone belt evolution. *Journal of African Earth Sciences*, 60 (5), p.346-352. DOI: 10.1016/j.jafrearsci.2011.03.012
- Kroner, A., Hegner, E., Wendt, J.I., and Byerly, G.R., 1996. The oldest part of the Barberton granitoid-greenstone terrain, South Africa: evidence for crust formation between 3.5 and 3.7 Ga. *Precambrian Research*, 78, p.105-124. DOI: 10.1016/0301-9268(95)00072-0
- Lowe, D.R., 1994. Accretionary history of the Archean Barberton greenstone belt (3.55-3.22

- Ga). *Southern Africa Geology*, 22, p.1099-1102. DOI: 10.1130/0091-7613(1994)022<1099:A-HOTAB>2.3.CO;2
- Maddox, L.M., Bancroft G.M., Scaini M.J., and Lorimer J.W., 1998. Invisible gold: Comparison of Au deposition on pyrite and arsenopyrite. *American Mineral*, 83(11), p.1240-1245. DOI: 10.2138/am-1998-11-1212
- McCaffrey, K.J.W., Lonergan, L., and Wilkinson, J.J., 1999. *Fractures, Fluid Flow and Mineralization. Geological Society of London, Special Publications*, 155pp.
- McLennan, S.M., Taylor, S.R., and Kroner, A., 1983. Geochemical evolution of Archean shales from South Africa. I. The Swaziland and Pongola Supergroups. *Precambrian Research*, 22 (1-2), p. 93-124. DOI: 10.1016/0301-9268(83)90060-8
- Mhlanga, G., 2002. *Data driven predictive modelling for Archean lode gold potential, Bubi greenstone belt, southwest Zimbabwe. M.Sc. Thesis* (unpublished), International Institute for Geo-Information Science and Earth Observation. Zimbabwe, 108pp.
- Middlemost, E.A.K., 1994. Naming materials in the magma/igneous rock system. *Earth Science Reviews*, 37 (3-4), p.215-224. DOI: 10.1016/0012-8252(94)90029-9
- Mikhlin, Y. and Romanchenko, A., 2007. Gold deposition on pyrite and the common sulphide minerals: An STM/STS and SR-XPS study of surface reactions and Au nanoparticles. *Geochimica et Cosmochimica Acta*, 71 (24), p.5985-6001. DOI: 10.1016/j.gca.2007.10.001
- Mikhlin, Y., Romanchenko, A., Likhatski, M., Karacharov, A., Erenburg, S., and Trubina, S., 2011. Understanding the initial stages of precious metals precipitation: Nanoscale metallic and sulfidic species of gold and silver on pyrite surfaces. *Ore Geology Reviews*, 42 (1), p.47-54. DOI: 10.1016/j.oregeorev.2011.03.005
- Mohammadnejad, S., Provis J.L., and Van Deventer, J.S.J., 2012. Reduction of gold (III) chloride to gold (0) on silicate surfaces, *Journal of Colloid and Interface Science*, 389 (1), p.252-259. DOI: 10.1016/j.jcis.2012.08.053
- Nance, W.B. and Taylor, S.R. 1977. Rare earth element patterns and crustal evolution-II. Archean sedimentary rocks from Kalgoorlie, Australia. *Geochimica et Cosmochimica Acta*, 41 (2), p.225-231. DOI: 10.1016/0016-7037(77)90229-0
- Ordóñez-Calderón, J.C., Polat, A., Fryer, B.J., Gagnon, J.E., Raith, J.G., and Appel, P.W.U., 2008. Evidence for HFSE and REE mobility during calc silicate metasomatism, Mesoarchean (~3075 Ma) Ivisartoq greenstone belt, southern West Greenland. *Precambrian Research*, 161, p.317-340. DOI: 10.1016/j.precamres.2007.09.004
- Otto, A., Dziggel, A., Kisters, A.F.M., and Meyer, F.M., 2007. The New Consort gold mine, Barberton greenstone belt, South Africa: orogenic gold mineralization in a condensed metamorphic profile. *Mineralium Deposita*, 42, p.715-735. DOI: 10.1007/s00126-007-0135-5
- Pitfield, P.E.J. and Campbell, S.D.G., 1996. Significance for gold exploration of structural styles of auriferous deposits in the Archean Bulawayo-Bubi greenstone belt of Zimbabwe. Transactions of the Institution of Mining and Metallurgy, section B. *Applied Earth Science*, 105 (5), p.41-52.
- Poujol, M. and Robb, L.J., 1999. New U-Pb zircon ages on gneisses and pegmatite from South of the Murchison greenstone belt, South Africa. *South African Journal of Geology*, 102 (2), p.93-97.
- Poujol, M., Robb, L.J., Anhaeusser, C.R., and Gericke, B., 2003. A review of the Geochronological constraints on the evolution of the Kaapvaal Craton, South Africa. *Precambrian Research*, 127, p.181-213. DOI: 10.1016/S0301-9268(03)00187-6
- Qian, G., Brugger, J., Skinner, W.M., Chen, G., and Pring, A., 2010. An experimental study of the mechanism of the replacement of

- magnetite by pyrite up to 300°C. *Geochimica et Cosmochimica Acta*, 74 (19), p.5610-5630. DOI: 10.1016/j.gca.2010.06.035
- Qian, G., Brugger, J., Testemale, D., Skinner, W., and Pring, A., 2013. Formation of As (II)-pyrite during experimental replacement of magnetite under hydrothermal conditions, *Geochimica et Cosmochimica Acta*, 100, p.1-10. DOI: 10.1016/j.gca.2012.09.034
- Ramdohr, P., 1958. New observations on the ores of the Witwatersrand in South Africa and their genetic significance. *Geological Society of South Africa*, LXI, 49pp.
- Raymond, L.A., 2002: *Petrology: The study of igneous, sedimentary and metamorphic rocks, 2nd*. McGraw-Hill Higher Education, Boston, MA.
- Reed, S.J.B., 1983. *Electron Microprobe Analysis, Applied Science Publishers Ltd.*, Analysis of High Temperature Materials, p.91-127.
- Reed, S.J.B., 2005. *Electron microprobe analysis and scanning electron microscopy in geology*, Cambridge University Press, New York, USA.
- Reich, M., Kesler S.E., Utsunomiya S., Palenik, C.S., Chryssoulis, S.L., and Ewing R.C., 2005. Solubility of gold in arsenian pyrite. *Geochimica et Cosmochimica Acta*, 69, p.2781-2796. DOI: 10.1016/j.gca.2005.01.011
- Rouchon, V., Orberger, B., Hofmann, A., and Pinti, D.L., 2009. Diagenetic Fe-carbonates in Paleoproterozoic felsic sedimentary rocks (Hooggenoeg Formation, Barberton greenstone belt, South Africa): Implications for CO₂ sequestration and the chemical budget of seawater. *Precambrian Research*, 172 (3-4), p.255-278. DOI: 10.1016/j.precamres.2009.04.010
- Saha, I. and Venkatesh, A.S., 2002. Invisible gold within sulphides from the Archaean Huttimaski schist belt, Southern India. *Journal of Asian Earth Sciences*, 20, p.449-457. DOI: 10.1016/S1367-9120(01)00050-5
- Schmitz, M.D., Bowring, S.A., De Wit, M., and Gartz, V., 2004. Subduction and terrane collision stabilize the western Kaapvaal Craton tectosphere 2.9 billion years ago. *Earth and Planetary Science Letters*, 222, p.363-376. DOI: 10.1016/j.epsl.2004.03.036
- Shaheen, M.E., Gagnon, J.E., and Fryer, B.J., 2012. Femtosecond (fs) lasers coupled with modern ICP-MS instruments provide new and improved potential for in situ elemental and isotopic analyses in the geosciences. *Chemical Geology*, 330-331, p.260-273. DOI: 10.1016/j.chemgeo.2012.09.016
- Stiegler, M.T., Lowe, D.R., and Byerly, G.R., 2010. The Petrogenesis of Volcaniclastic Komatiites in the Barberton Greenstone Belt, South Africa: a textural and Geochemical Study. *Journal of Petrology*, 51, p.947-972. DOI: 10.1093/petrology/egq008
- Sung, Y.H., Brugger J., Ciobanu L., Pring A., Skinner W., and Nugus M., 2009. Invisible gold in arsenian pyrite and arsenopyrite from a multistage Archaean gold deposit: Sunrise Dam, Eastern Goldfields Province. *Western Australia Mineral Deposita*, 44, p.765-791. DOI: 10.1007/s00126-009-0251-5
- Sylvester, P.J., Cabri, L.J., Tubrett, M.N., McMahon, G., Laflamme, J.H.G., and Peregoedova, A., 2005, Synthesis and evaluation of a fused pyrrhotite standard reference material for platinum group element and gold analysis by laser ablation-ICPMS. In: Törmänen, T.O., and Alapieti, T.T. (eds.), 10th International Platinum Symposium: Oulu, *Geological Survey of Finland, Extended Abstracts*, p.16-20.
- Sylvester, P.J., 2008. *Laser ablation-ICP-MS in the earth sciences: Current practices and outstanding issues. Mineralogical Association of Canada*, 348pp.
- Thèbaud, N., Philippot, P., Rey, P., Brugger, J., Van Kranendonk, M., and Grassineau, N., 2008. Protracted fluid-rock interaction in the Mesoarchaean and implication for gold mineralization: Example from the Warrawoona syncline (Pilbara, Western Australia). *Earth and Planetary Science Letters*, 272 (3-4), p.639-655. DOI: 10.1016/j.epsl.2008.05.030

- Thomas, R., 2005: *Practical Guide to ICP-MS*. Marcel Dekker Inc. New York, USA, 62, 393pp.
- Toulkeridis, T., Clauer, N., Kroner, A., Reimer, T., and Todt, W., 1999. Characterization, provenance, and tectonic setting of the Fig Tree greywackes from the Archaean Barberton Greenstone Belt, South Africa. *Sedimentary Geology*, 124, p.113-129. DOI: 10.1016/S0037-0738(98)00123-7
- Vaughan, J.P. and Kyin, A., 2004. Refractory gold ores in Archaean greenstones, Western Australia: mineralogy, gold paragenesis, metallurgical characterization and classification. *Mineralogical Magazine*, 68 (2), p.255-277. DOI: 10.1180/0026461046820186
- Viljoen, M.J. and Viljoen, R.P., 1969. An introduction to the geology of the Barberton granite-greenstone terrain. Upper Mantle Project. *Special Publication Geological Society of South Africa*, 2, p.9-28.
- Ward, J.H.W., 1995. Geology and metallogeny of the Barberton greenstone belt: a survey. *Journal of Africa Earth Sciences*, 21, p.213-240.
- Ward, J.H.W., 1999. The metallogeny of the Barberton Greenstone Belt, South Africa and Swaziland. *Geological Survey of South Africa, Memoir*, 21 (2), p.213-240. DOI: 10.1016/0899-5362(95)00067-4
- Watling, R.J. and Herbert, H.K., 1994. Gold fingerprinting by laser ablation inductively coupled plasma mass spectrometry, *Spectrochimica Acta*, 499 (2), p.205-219. DOI: 10.1016/0584-8547(94)80019-7
- Watson, J.S., 1996. Fast, Simple Method of Powder Pellet Preparation for X-Ray Fluorescence Analysis. *X-Ray Spectrometry*, 25, p.173-174. DOI: 0.1002/(SICI)-1097-4539(199607)25:4<173::AID-XRS15-8>3.0.CO;2-Z
- Williams, P.J., 1997. A metamorphosed, strata-bound-epigenetic origin for a gruneritic Archean gold deposit, Barberton, South Africa. *Ore Geology Reviews*, 12, p.135-151. DOI: 10.1016/S0169-1368(97)00006-1
- Winderbaum, L., Ciobanu C.L., Cook, N.J., Paul, M., Metcalfe, A., and Gilbert, S., 2012. Multivariate Analysis of an LA-ICP-MS Trace Element Dataset for Pyrite. *International Association for Mathematical Geosciences*, 44, p.823-842. DOI 10.1007/s11004-012-9418-1.
- Woodhead, J., Hergt, J., Meffre, S., Large, R.R., Danyushevsky, D., and Gilbert, S., 2009. In situ Pb-isotope analysis of pyrite by laser ablation (multicollector and quadrupole) ICPMS. *Chemical Geology*, 262, p.344-354. DOI: 10.1016/j.chemgeo.2009.02.003
- Yoshihara, A. and Hamano, Y., 2004. Paleomagnetic constraints on the Archean geomagnetic field intensity obtained from komatiites of the Barberton and Belingwe greenstone belts, South Africa and Zimbabwe. *Precambrian Research*, 131, p.111-142. DOI: 10.1016/j.precamres.2004.01.003
- Zachariáš, J., Frýda, J., Paterová, B., and Mihaljevič, M., 2004. Arsenopyrite and As-bearing pyrite from the Roundý deposit, Bohemian Massif. *Mineralogical Magazine*, 68, p.31-46. DOI: 10.1180/0026461046810169
- Zhao, H.X., Frimmel, H.E., Jiang, S.Y., and Dai, B.Z., 2011. LA-ICP-MS trace element analysis of pyrite from the Xiaoqinling gold district, China: Implications for ore genesis, *Ore Geology Reviews*, 43, p.142-153. DOI: 10.1016/j.oregeorev.2011.07.006